Composites Communications 60 (2025) 102654

Contents lists available at ScienceDirect

Composites Communications

journal homepage: www.elsevier.com/locate/coco

Mode II fracture behavior of CF/PEKK composites with open-hole and bolted joint geometries at high-temperatures

Kyo-Moon Lee [a], Sanjay Kumar [a], Sung-Won Yoon [b], Chang-Wook Park [b], Nao-Aki Noda [c], Yun-Hae Kim [a,*]

[a] Dept. of Ocean Advanced Materials Convergence Engineering, Korea Maritime and Ocean University, 727 Taejong-ro, Yeongdo-gu, Busan, 49112, Republic of Korea
[b] Dept. of Advanced Materials, Research Institute of Medium & Small Shipbuilding(RIMS), 38-6 Noksansandan 232-ro, Gangseo-gu, Busan, 46757, Republic of Korea
[c] Kyushu Institute of Technology, 1-1 Sensui-cho, Tobata-ku, Kitakyushu-shi, Fukuoka, Japan

ARTICLE INFO

Keywords:
CF/PEKK composites
Mode II fracture behaviour
Open hole
Bolted joints

ABSTRACT

Despite the growing interest in carbon fiber-reinforced polyetherketoneketone (CF/PEKK) composites, the combined effects of temperature and geometric configuration on Mode II apparent fracture toughness (G_{IIc}^{app}) remain insufficiently understood. This study investigates the influence of open-hole (OH) and bolted joint (BJ) configurations on the G_{IIc}^{app} and failure mechanisms of CF/PEKK composites. Unidirectional laminates were tested using the end-notched flexure method, with variables including width-to-hole diameter ratios (W/D = 3.3, 6.6), crack–hole distance (L = 5, 10, 15, 20 mm), and temperature (25 °C, 110 °C, 150 °C).

According to the results, geometry (W/D, L) and temperature jointly govern the Mode II fracture behavior of CF/PEKK, with OH reducing the apparent toughness while BJ compensates for a substantial portion of this loss. In high-temperature environments, viscoelastic behavior–induced matrix softening influences crack initiation, propagation and the transition of failure modes. For W/D = 3.3, crack initiation is locally triggered as L decreases, and rising temperature can accelerate initiation due to PEKK softening. As the temperature approaches T_g, local bending deformation induced by the OH configuration precedes crack growth and then transitions to mixed-mode (Mode I + II), leading to a change in the failure mechanism. BJ are limited in their ability to constrain the crack; however, compressive stresses within the BJ zone increase interfacial friction, restoring effective crack initiation and propagation behavior. These results highlight the importance of considering both geometric and thermal conditions for the reliable joint design of CF/PEKK structures.

1. Introduction

Thermoplastic composites offer recyclability, ease of repair, and high impact resistance, making them attractive alternatives to thermosets in aerospace and automotive sectors [1]. Among them, carbon fiber reinforced polyetherketoneketone (CF/PEKK) composites exhibits outstanding mechanical performance [2], high-temperature stability [3], and chemical resistance, positioning it for next-generation structural applications [4,5].

In composite structures, assembly methods such as bolted joints (BJ), rivets, and open holes (OH) introduce geometric discontinuities that alter local stress fields and create stress concentrations, which can initiate delamination and accelerate crack growth [6]. In addition to serving as local initiation sites, such discontinuities may also accelerate the propagation of cracks originating from external sources once they extend into these regions, thereby amplifying structural vulnerability. This progressive damage mechanism reduces structural stiffness, interrupts load transfer paths, and shortens service life, ultimately posing significant challenges to structural integrity in safety-critical fields such as aerospace and automotive engineering [7–10].

The effect of geometric discontinuities on composite structural behavior has been extensively studied, with a focus on stress concentration, delamination onset, and load-bearing degradation. Eksi et al. [11]evaluated the reductions in tensile strength and elastic modulus of CFRP laminates as functions of hole diameter, count, and fiber orientation, and confirmed local damage initiation around holes. Numerous studies [12–15] similarly report that OH frequently acts as a delamination origin, with load redistribution promoting interfacial failure. Prior work is biased toward tensile and compressive loading and tends to focus on hole-initiated damage. However, when externally originated

* Corresponding author.
E-mail address: yunheak@kmou.ac.kr (Y.-H. Kim).

https://doi.org/10.1016/j.coco.2025.102654
Received 16 September 2025; Received in revised form 9 November 2025; Accepted 21 November 2025
Available online 23 November 2025

cracks interact with OH and notches, the Mode I/II interfacial delamination behavior—and the associated fracture toughness—remains insufficiently understood.

BJ serves not only as a mechanical fastener but also as a critical structural element that influences load transfer, stress distribution, and failure behavior in composite assemblies. Optimizing design variables and understanding their effects on failure mechanisms are essential for durability and reliability [10].

In CF/PEKK composite structures, geometric parameters of BJ—such as the width-to-diameter ratio (W/D)—govern load-bearing performance and changes in failure mode (from net-tension to bearing-dominated failure) [16,17]. These geometric factors can, during crack initiation and propagation, promote interlaminar delamination through crack–BJ/OH interaction, leading to structural failure in laminated thermoplastic composites. However, under these conditions, their behavior under fracture-driven conditions—particularly interlaminar delamination resistance in Mode I and Mode II—has received limited attention.

Cheung et al. [18–20] found that under Mode I loading, mechanical fasteners can suppress crack propagation by closing the crack tip or applying clamping pressure. Under Mode II, crack-arrest capacity is more limited, as crack-face friction and local stiffness mainly delay, rather than suppress, interfacial crack growth. Hole diameter and location also significantly affect Mode I and II energy release rates, underscoring the sensitivity of delamination behavior to joint design [21,22]. These studies have focused on brittle thermoset composites; therefore, research on comparatively ductile CF/PEKK thermoplastic composites is important. In this context, this study provides a novel contribution by systematically investigating Mode II delamination resistance in thermoplastic CF/PEKK laminates featuring BJ and OH configurations.

Temperature significantly affects the mechanical behavior and failure modes of thermoplastic composites and is essential for ensuring structural reliability.

In CF/PEKK composites, temperature-dependent changes in mechanical performance—such as tensile strength, bearing capacity, and failure mode—have been reported under BJ configurations across −60 °C, 25 °C, and 200 °C [16,17]. These studies showed that high temperatures induced matrix softening, resulting in reduced strength but enhanced deformability due to increased ductility. In contrast, low temperatures caused matrix embrittlement, leading to early failure and diminished fracture resistance.

Temperature also influences fracture resistance, influencing energy dissipation and crack growth. Studies show fracture toughness remains relatively stable below the glass transition temperature (T_g), but is reduced above it due to matrix softening or interfacial weakening [23,24]. Thermoplastics such as GF/PP show notable reductions in Mode I toughness and bridging capacity under moderate thermal conditions [25], whereas slightly elevated temperatures may enhance ductility and energy absorption in some epoxy-based systems [26]. Most temperature-related studies focus on thermoset composites and defect-free specimens.

The interactive effects of temperature and geometric discontinuities remain largely unexplored. From these findings, W/D and hole location—by modifying the load-transfer mechanism at or around the hole through OH/BJ—govern Mode-II behavior. At temperatures near T_g, the matrix's viscoelastic response is amplified, leading to property degradation; accordingly, thermal degradation effects, as conditioned by the OH geometry, are expected to influence the crack-tip FPZ and its interaction with the hole, as well as the stability of crack initiation/propagation and the resulting crack path. These opinions highlight the complexity and material dependency of temperature effects on fracture behavior, underscoring the need for further investigation under Mode II in high-performance thermoplastics.

To the best of our knowledge, prior work shows limitations: (i) OH studies have focused predominantly on tensile/compressive loading; (ii) delamination research has emphasized hole-initiated damage or omitted OH entirely; and (iii) the coupling between temperature and OH has rarely been examined.

Accordingly, this study is the first to systematically examine G_{IIc}^{app}, Mode II delamination behavior, and failure mechanisms in CF/PEKK laminates with BJ and OH configurations under elevated temperatures (25 °C, 110 °C, 150 °C), providing new insights into fracture mechanisms in thermoplastic composite structures and expected to promote further innovation in high-performance engineering applications.

2. Experimental

2.1. Materials and specimens

For the Mode II test, unidirectional CF/PEKK prepreg was stacked in a $[0]_{24}$ configuration, and panels were manufactured using a vacuum bag-only process. Details of the fabrication information procedure are shown in Fig. 1a. To evaluate the internal quality of the manufactured panels, void content was measured following ASTM D2734 and optical microscopy (OM) analysis. The average void volume fraction was 1.14 ± 0.3 % by ASTM D2734 and approximately 0.9 ± 0.2 % by OM observation, confirming high consolidation quality. Specimen fabrication followed ASTM D7905. A schematic of the no-hole, OH, and BJ geometries, as well as Mode II test specimens, is shown in Fig. 1a, b. Variables included W/D ratios of 6.6 and 3.3 (hole diameters 3 and 6 mm), crack–hole distances (L) of 5, 10, 15, and 20 mm, and test temperatures of 25 °C, 110 °C, and 150 °C (close to T_g = 158 °C). The hole machining, fastening methods, and quality control measures were consistent with previous studies [27].

2.2. Test setup

Mode II behavior was evaluated by end-notched flexure (ENF) tests (ASTM D7905) in a three-point bending configuration on a universal testing machine (Instron, USA) at 0.5 mm/min. Environmental tests were conducted after the specimens were stabilized at the target temperature, followed by testing in the Instron chamber. A series of 5 specimens was tested in each configuration in order to obtain a statistically representative average of the mode II behavior. All tests were recorded on video for digital image correlation (DIC, GOM ARAMIS, Germany) and crack propagation analysis. Morphological analyses of the fracture surface were conducted with high-resolution 3D optical microscopy (VHX-7000, Keyence, Osaka, Japan) and scanning electron microscope (SEM, CLARA, Tescan Co., Ltd., Czech). Dynamic Mechanical Analysis (DMA) was performed to evaluate the viscoelastic behavior of CF/PEKK (HR 30 Discovery Hybrid Rheometer, Waters Corporation, USA). The test was conducted at a constant strain of 0.1 % and frequency of 1Hz, with the temperature increased from 25 °C to 160 °C at a heating rate of 1 °C/min.

2.3. Data-reduced method and calculation

It should be noted that the fracture toughness reported in this study represents apparent fracture toughness (G_{IIc}^{app}), reflecting the influences of OH, BJ, and temperature, rather than intrinsic fracture toughness. The Mode II fracture toughness is determined by the fracture energy (G) for a crack growth and can be derived from Irwin-Kies equation:

$$G = \frac{P^2}{2B}\frac{dC}{da} \tag{1}$$

where P is the applied load, B is the specimen width. However, in ENF tests, accurate measurement of the actual crack length (a) is difficult due to the fracture processing zone (FPZ) and micro-damage near the crack tip. Therefore, this study employs the CBBM [28,29], which relies on the equivalent crack length (a_e) approach and represents crack growth

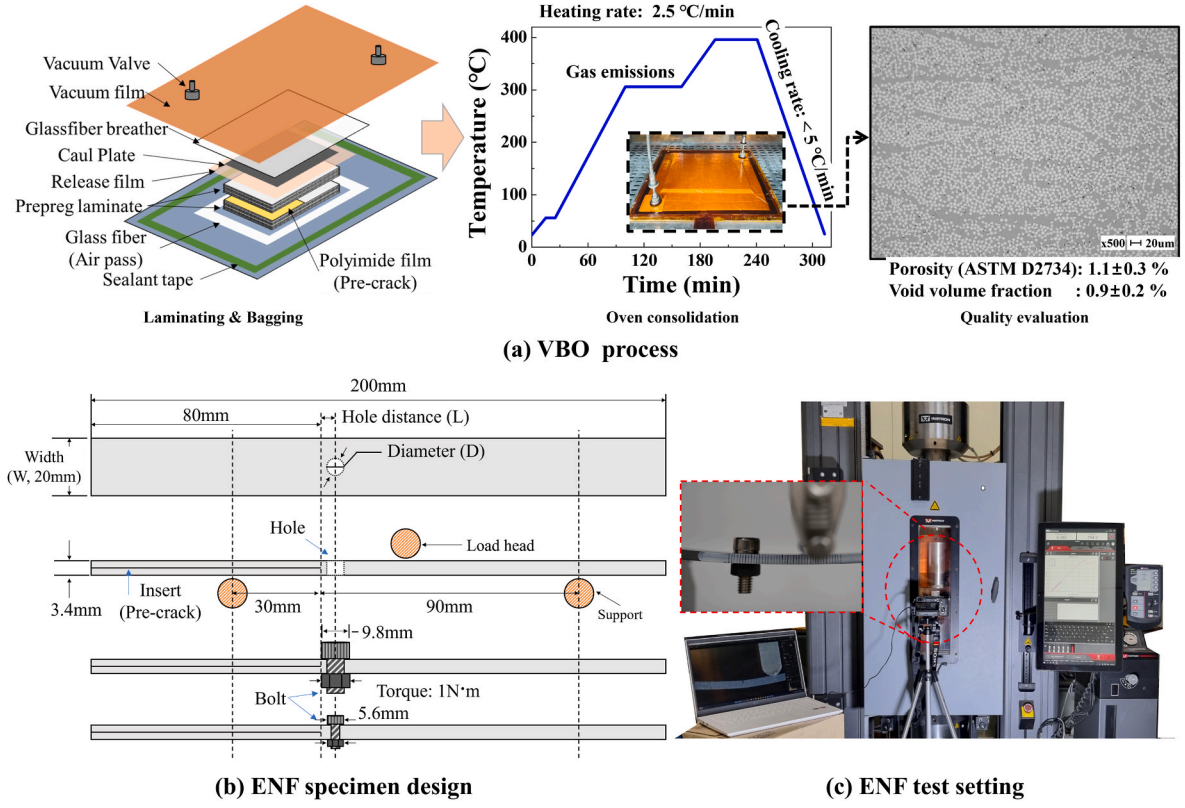

Fig. 1. (a) Schematic illustration of the geometries for the no-hole, open-hole, and bolted-joint specimens, and (b) Mode II test configuration.

solely through specimen compliance. The load-point compliance C can be given by:

$$C = \frac{\delta}{P} = \frac{3a_e^3 + 2L^3}{8E_f Bh^3} + \frac{3L}{10BhG_{13}} \tag{2}$$

Where δ is the displacement, h is the half-thickness of the laminate, I is the second moment of area, L is the half-span length, E_f and G_{13} are the flexural and shear modulus. To account for the FPZ effect on compliance, E_f was used. It can be estimated for each specimen from the initial compliance (C_0) and initial crack (a_0):

$$E_f = \frac{3a_0^3 + 2L^3}{8Bh^3}\left(C_0 - \frac{3L}{10G_{13}Bh}\right)^{-1} \tag{3}$$

And, The FPZ is a region near the crack tip where various damage mechanisms, such as micro-cracking, fiber-matrix interfacial debonding, and fiber bridging, occur. In this zone, nonlinear material behavior becomes prominent, serving as a major factor in resisting crack propagation. Therefore, the size and characteristics of the FPZ have a direct influence on the fracture toughness. To account for this FPZ effect in the compliance formulation, a_e is introduced to replace a. The a_e is given by:

$$a_e = a + FPZ = \left[\frac{C_{corr}}{C_{0\_corr}}a_0^3 + \frac{2}{3}\left(\frac{C_{corr}}{C_{0\_corr}} - 1\right)L^3\right]^{\frac{1}{3}} \tag{4}$$

where C_{corr}, C_{0_corr} is given by Eq. (4), (5) respectively

$$C_{corr} = C - \frac{3l}{10G_{13}Bh} \tag{6}$$

$$C_{0\_corr} = C_0 - \frac{3l}{10G_{13}Bh} \tag{7}$$

Finally, the Mode II fracture energy is calculated from Eqs. (1) and (2) as:

$$G_{IIC} = \frac{9P^2a_e^2}{16B^2E_fh^3} \tag{8}$$

The CBBM method allows for the determination of G_{IIc} using only the L–D curve, eliminating the need to measure crack length during propagation. Additionally, the equivalent crack length, a_e, accounts for FPZ effects, unlike when the actual crack length is used. The G_{13} was taken from the manufacturer's datasheet (5.2A GPa at 25 °C, 3.9 GPa at 110 °C; 3.9 GPa was assumed at 150 °C). Since G_{13} is only a secondary parameter in the CBBM equation, these variations have a negligible influence on the calculated G_{IIc}^{app} [30]. Additionally, the absorbed energy (E_{abs}, up to crack initiation) was calculated by integrating the area under the load-displacement curve.

3. Results and discussion

3.1. Effect of temperature on mode II properties of CF/PEKK

The Mode II Behavior of CF/PEKK specimens without OH is presented in Fig. 2, showing exposure temperature-dependent trends in the load–displacement (L-D) curves, maximum load, E_f, and G_{IIc}^{app}. At 25 °C, the L–D curves exhibited a linear increase in load to the maximum value (Fig. 2a), followed by a sudden drop, indicating brittle failure behavior. At elevated temperatures (110 °C and 150 °C), nonlinear deformation initiated earlier (arrows in Fig. 2a), and compliance increased near the maximum load, after which the load decreased more gradually. This transition is attributed to matrix softening, as evidenced by the temperature-dependent decrease in storage modulus (G′) and the rise in loss modulus (G″) observed in the DMA results (Fig. 3) [31,32]. These viscoelastic changes reduce the interlaminar shear strength [3]—a critical factor governing Mode II delamination [33–35]—thereby facilitating crack initiation and propagation [36–39], and shifting the failure mechanism from brittle to quasi-brittle or progressive interlaminar

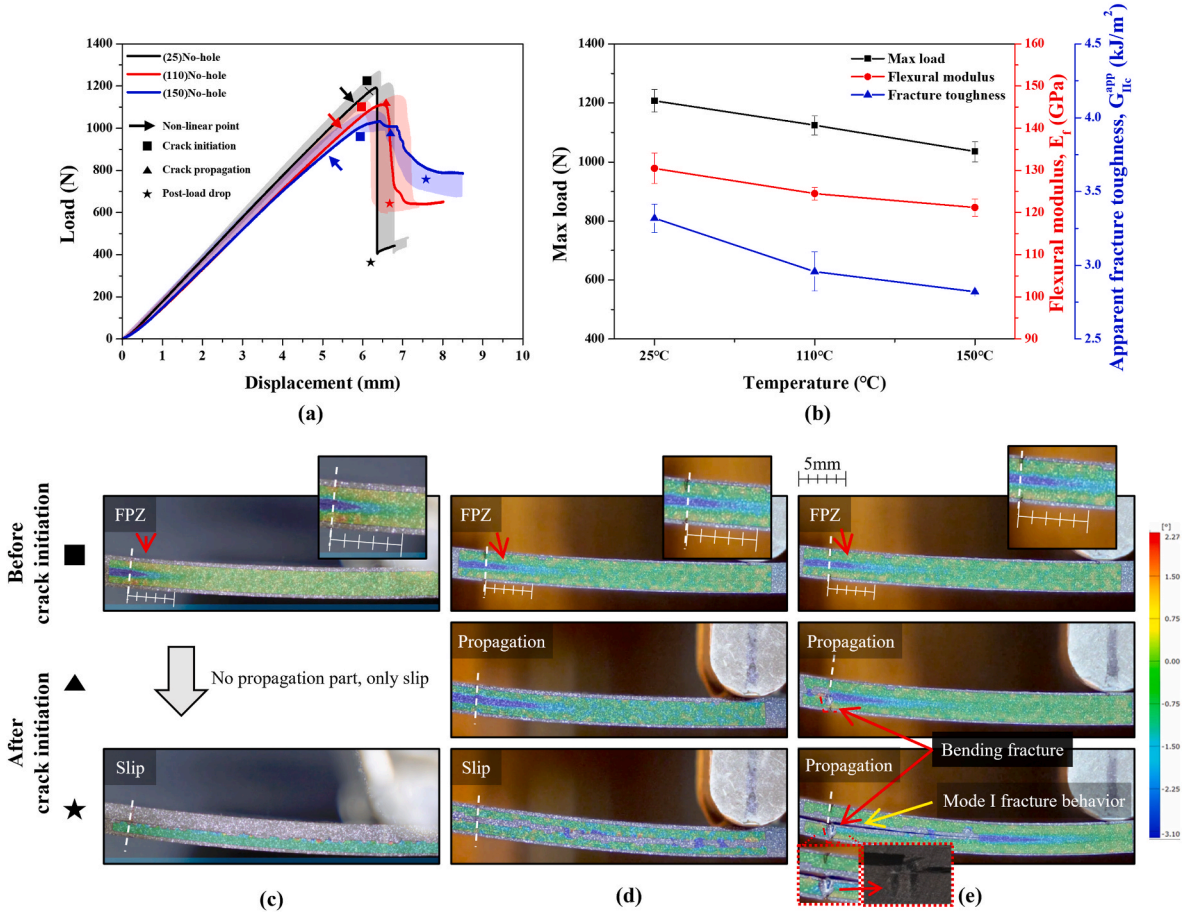

Fig. 2. Mode II behavior of no-hole specimens under increasing temperature: (a) load–displacement (L–D) curves; (b) maximum load, flexural modulus, and fracture toughness; (c–d) DIC-based strain distributions near the crack tip during propagation at different points along the L–D curve.

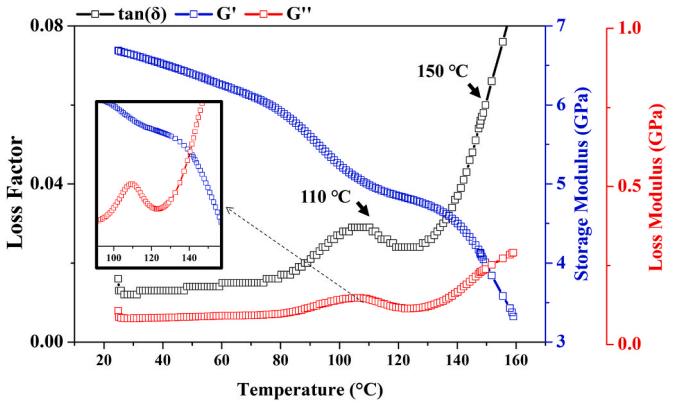

Fig. 3. Temperature-dependent Dynamic Mechanical Analysis (DMA) results of CF/PEKK composites showing transition from elastic to viscoelastic response starting at 80 °C, with a primary G′ peak at 110 °C.

shear failure. This transition is further supported by SEM observations (Figs. 6, 9 and 10), where elevated temperatures led to ductile matrix deformation and more pronounced fiber imprints at the crack tip.

This interpretation is supported by the quantitative results shown in Fig. 2b. At 25 °C, the CF/PEKK demonstrated the highest performance, with a maximum load of 1207 N and a E_f of 130 GPa. As the temperature approached T_g, both values declined to 1124 N and 124 GPa at 110 °C, and to 1035 N and 121 GPa at 150 °C (ref. Table 1).

In addition, Temperature affected crack propagation, progressively suppressing the sudden drop observed at 25 °C. This behavior is attributed to the development of a more extensive FPZ, which redistributes stress and spreads damage, thereby enabling gradual energy dissipation instead of sudden interlaminar fracture.

Fig. 2c–e presents DIC analyses of the strain distributions near the crack tip at representative points (■-★ in Fig. 2a) on the L5 L–D curve under each temperature condition. At 25 °C (Fig. 2c), the DIC strain maps, corresponding to the FPZ, reveal a sharply confined shear-dominated region just ahead of the crack tip, followed by a rapid slip event that propagates toward the load point. In contrast, at 110 °C (Fig. 2d), the DIC strain maps reveal a wider FPZ ahead of the crack tip compared with 25 °C. The enlarged FPZ promotes more stable crack initiation and progressive propagation, during which the extended crack growth allows greater energy dissipation within the FPZ. Consequently, slip occurs at a later stage, resulting in a smaller load drop in L-D curve.

At 150 °C (Fig. 2e), the FPZ and overall crack propagation behavior are similar to those at 110 °C. However, during propagation, localized plastic deformation—particularly bending fracture—occurred near the pre-crack tip, producing interlaminar shear and opening failure. This mixed-mode damage dissipated energy at the crack tip, further moderating the load reduction.

The temperature-dependent fracture behavior—characterized by matrix softening and mixed-mode propagation—significantly influenced the G_{IIc}^{app} of CF/PEKK composites. At 110 °C, G_{IIc}^{app} decreased to 2.96 kJ/m^2, which is 10.8 % lower than 25 °C (3.32 kJ/m^2), while at 150 °C it further declined to 2.82 kJ/m^2 (15.1 % reduction), yet both remained relatively high considering the proximity to T_g (158 °C). Compared with literature values for thermoset and thermoplastic composites, which often drop >30 % near T_g [34,38,40–42], these results

Table 1
Experimental results for each condition.

Conditions				Test temperature								
				25 °C			110 °C			150 °C		
Name	OH/BJ	W/D	L	Max Load (N)	E_f (GPa)	G_{IIc}^{app} (kJ/m^2)	Max Load (N)	E_f (GPa)	G_{IIc}^{app} (kJ/m^2)	Max Load (N)	E_f (GPa)	G_{IIc}^{app} (kJ/m^2)
No-Hole	–	–	–	1208 ± 38	130.5 ± 3.6	3.32 ± 0.1	1124 ± 33	124.5 ± 1.5	2.96 ± 0.13	1035 ± 34	121.2 ± 2.1	2.82 ± 0.1
L5H3	OH	6.6	5	1142 ± 36	126.1 ± 1.3	2.99 ± 0.2	994 ± 29	129.8 ± 2.5	2.28 ± 0.1	879 ± 43	116.7 ± 1.7	2.24 ± 0.2
L10H3			10	1152 ± 31	125.2 ± 2.1	3.22 ± 0.12		–			–	
L15H3			15	1217 ± 45	124.1 ± 0.3	3.58 ± 0.21	1121 ± 47	129.2 ± 1.8	3.04 ± 0.2	795 ± 41	116.3 ± 3.1	–
L20H3			20	1170 ± 30	124.1 ± 1.1	3.4 ± 0.1		–			–	
L5H6		3.3	5	977 ± 53	123.4 ± 3.4	2.25 ± 0.34	818 ± 32	120.9 ± 3.6	1.66 ± 0.12	722 ± 26	110.7 ± 1.7	1.67 ± 0.12
L10H6			10	1145 ± 27	122.1 ± 1.5	3.11 ± 0.25		–			–	
L15H6			15	1166 ± 17	121.9 ± 2.7	3.53 ± 0.1	1085 ± 17	121.9 ± 2.8	3.28 ± 0.07	677 ± 9	108.7 ± 2.1	–
L20H6			20	1150 ± 58	117.3 ± 0.7	3.47 ± 0.2		–			–	
L5H3	BJ	6.6	5	1169 ± 22	125.2 ± 1.2	3.43 ± 0.17	1060 ± 38	129.3 ± 2.7	2.8 ± 0.28	944 ± 33	119.7 ± 0.5	2.57 ± 0.21
L15H3			15	1204 ± 28	128.9 ± 1.9	3.44 ± 0.17	1082 ± 35	128.3 ± 3	3.01 ± 0.09	914 ± 33	119.5 ± 0.3	-
L5H6		3.3	5	1157 ± 14	127.2 ± 2.1	3.12 ± 0.09	908 ± 14	124.1 ± 1.8	2.16 ± 0.12	840 ± 16	113.6 ± 1.5	2.27 ± 0.15
L15H6			15	1168 ± 30	122.3 ± 0.8	3.85 ± 0.2	1103 ± 74	122.8 ± 2.7	3.25 ± 0.25	775 ± 42	110.6 ± 1.5	–

highlight the superior thermal stability of CF/PEKK. This performance is attributed to matrix softening and stiffness reduction at elevated temperatures, which facilitate out-of-plane deformation under bending and induce local tensile stresses that contribute to partial Mode I behavior (Fig. 2e).

The relatively high G_{IIc}^{app} at 150 °C reflects increased energy absorption from this fracture mode transition and matrix compliance, not overestimation. Since CBBM derives G_{IIc}^{app} from the L–D response, it inherently captures such nonlinear effects, making it well-suited for thermoplastics exhibiting mixed-mode behavior under different temperatures. Overall, temperature-induced matrix softening alters crack initiation and propagation, yet CF/PEKK retains high fracture toughness, indicating robust interlaminar resistance. These findings underscore the need to account for temperature effects when designing CF/PEKK structures for thermal service environments.

3.2. Mode II properties of open hole CF/PEKK

3.2.1. Influence of geometry on mode II behavior at room temperature

The Mode II test results for different geometric configurations are shown in Fig. 4, including L–D curves, maximum load, and E_f. In Fig. 4a and b, OH specimens exhibited L–D behavior similar to no-hole specimens, with a linear increase up to the maximum load followed by slip. Despite this similarity, the presence of a hole significantly affected both the maximum load and E_f. Specifically, for L5 W/D = 6.6 condition, the maximum load and E_f were 1141 N and 127 GPa, representing reductions of 5.4 % and 2.1 %, respectively, compared to the no-hole condition (Fig. 4c and d). These reductions at W/D = 3.3 became more pronounced, reaching 19.1 % and 6.4 %, respectively. Increasing L significantly influenced the mechanical response; it caused the maximum load to gradually approach the no-hole value, indicating reduced sensitivity to the hole.

The reduction in maximum load is attributed to the interaction between the hole's stress field and the FPZ at the crack tip. When L is small, these fields overlap, intensifying local stress concentration and causing unstable crack growth and early failure before the critical load [43,44]. Similarly, Konieczny et al. [45] reported that stress field interference between multiple holes increases the stress concentration factor compared to a single-hole configuration. Conversely, when the hole is sufficiently distant from the FPZ, the interaction becomes negligible, allowing stable crack initiation and contributing to partial recovery of the Mode II behavior. However, when the hole is closer to the loading point, L20, compliance near the L–D curve peak increases. This behavior indicates deformation before crack initiation, which leads to a lower maximum load. Consistent with this interpretation, Section 3.3.2 (Fig. 7b) shows that, at W/D = 3.3, the L15 and L20 specimens exhibit off-axis damage around the hole. This behavior indicates that the hole vicinity can accommodate deformation while still bearing load—prior to crack initiation—thereby increasing compliance and altering the near-peak portion of the L–D response.

However, E_f was mainly governed by W/D, and variations in L had no notable effect on the overall flexural modulus. However, when the hole was positioned close to the loading point (L20), a distinct bending response was observed, accompanied by a slight decrease in E_f

This E_f reduction is further compounded by geometric effects; specifically, W/D decreasing raises the stress concentration factor [46]and fiber discontinuity, causing fiber breakage or distortion that increases local anisotropy [47]. Under Mode II loading, where tensile stresses and compressive stresses are applied simultaneously around the hole, these geometric and microstructural effects combine to intensify local stress concentration, leading to a substantial reduction in overall flexural performance even when the crack-tip position remains constant [48].

To analyze crack tip–hole interaction, Fig. 5 presents FPZ behavior near the crack tip on the L–D curve, a schematic illustrating FPZ–hole interference, and the FPZ length for each OH configuration (using Eq. (3)). In Fig. 5a, all specimens showed similar FPZ initiation, but L5 with W/D = 3.3 exhibited an earlier onset of nonlinearity and accelerated FPZ growth, suggesting strong crack tip - hole interaction. The W/D =

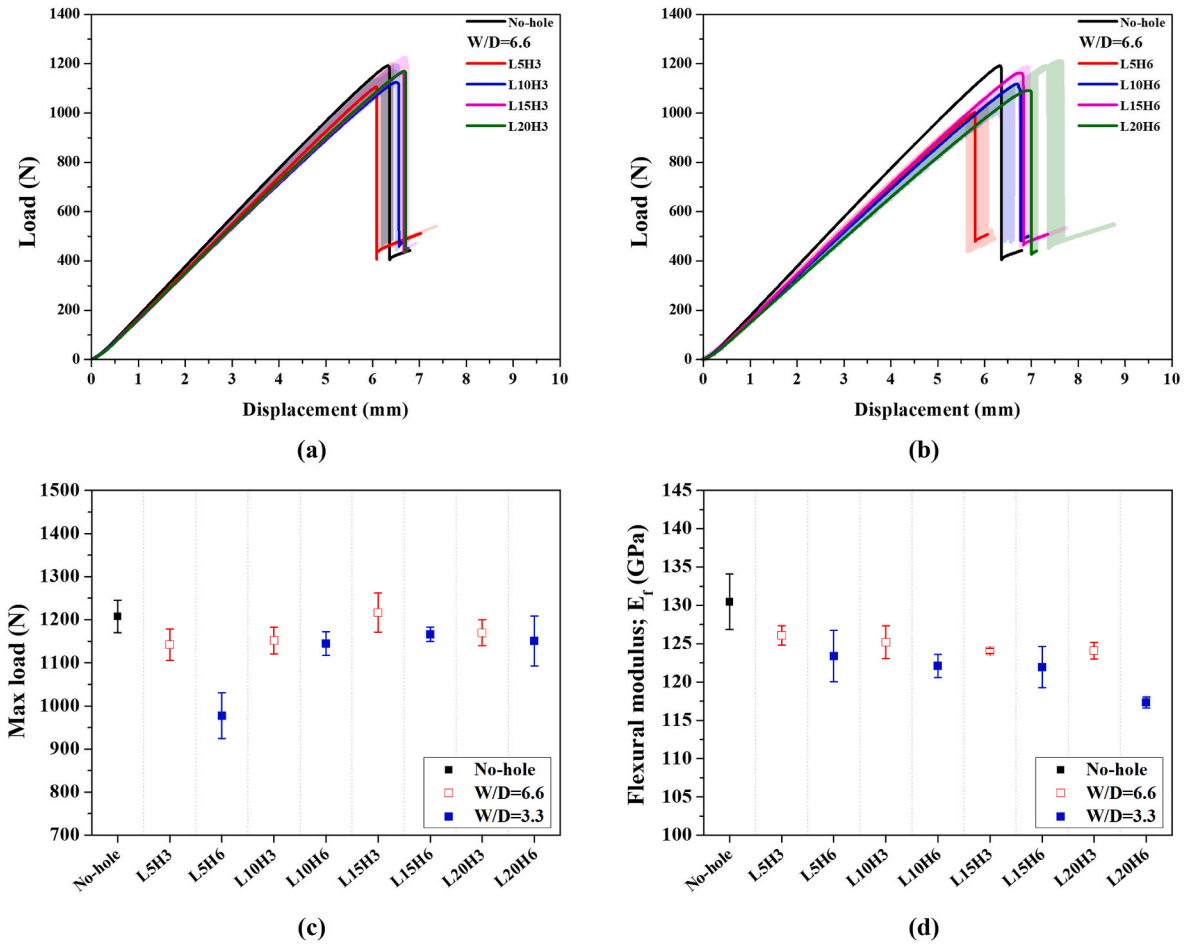

Fig. 4. Mode II behavior as different W/D and L: (a,b) load–displacement curve, (c) maximum load, (d)flexural modulus.

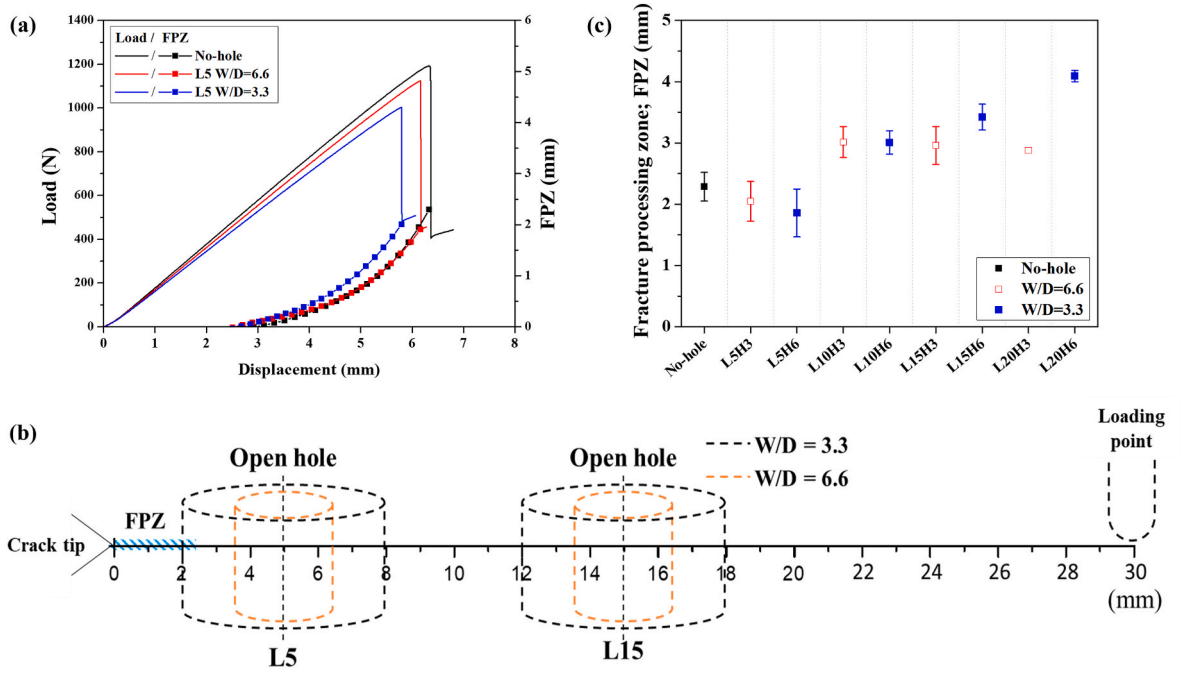

Fig. 5. Fracture process zone (FPZ) characteristics according to open hole (OH) geometry: (a) FPZ formation process indicated on the load–displacement curve, (b) Correlation between FPZ length and OH configuration, and (c) Comparison of FPZ lengths for each geometric condition.

6.6 showed a response similar to the no-hole condition, indicating limited interaction. These trends match the maximum load reduction in Fig. 4. This interaction is further illustrated in Fig. 5b. The FPZ of no-hole is approximately 2.3 mm. In the L5 configuration, the hole lies in close proximity to this FPZ, allowing interference between their stress fields, which intensifies local stress and accelerates crack initiation. For L10 and L15, the holes are located beyond the FPZ, reducing stress field overlap and allowing stable crack growth. This is consistent with the fracture surface presented in Section 3.2.2. Beyond L5, the FPZ length increased relative to the no-hole condition, and for W/D = 3.3, it continued to increase. The FPZ is influenced by compliance, and that estimated from the CBBM model reflects both crack-tip fracture processes and local deformation. This enlargement suggests that holes positioned closer to the loading point exhibit greater sensitivity to bending-induced deformation.

3.2.2. *Influence of geometry on fracture behavior at room temperature*

Fig. 6 illustrates crack propagation behavior and fracture surface at

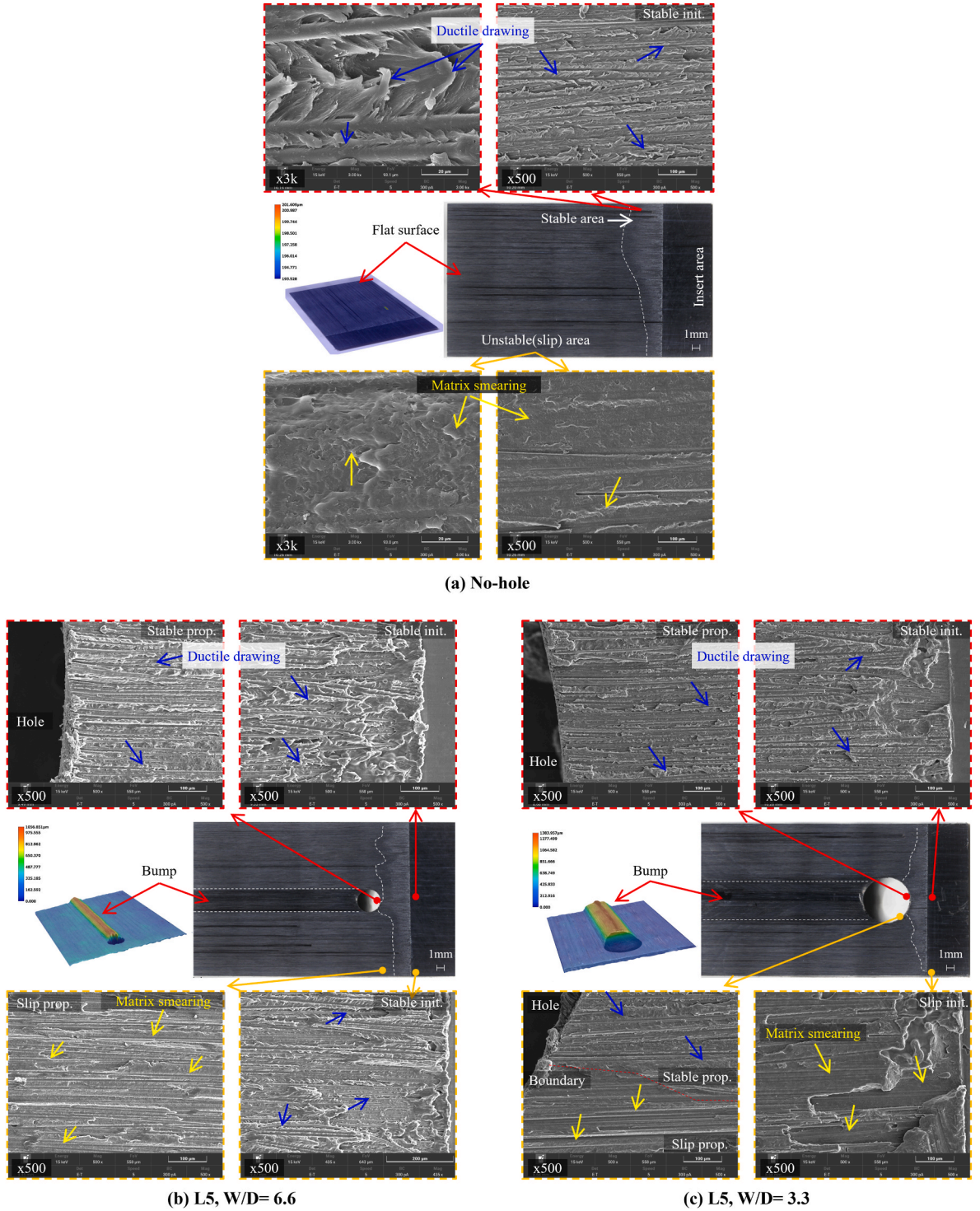

Fig. 6. Fracture surfaces of CF/PEKK specimens with different open-hole geometries at 25 °C, observed by OM and SEM: (a) no-hole, (b) L5, W/D = 6.6, (c) L5, W/D = 3.3; accelerated localized crack growth around the hole.

25 °C for various W/D ratios. FPZ of approximately 2–3 mm formed at the crack tip and promotes stable behavior in the no-hole specimen (Fig. 6a OM). This is consistent with the FPZ development shown in Fig. 5a. The FPZ fracture surface was dominated by ductile drawing from shear, while the slip region exhibited matrix smearing with a relatively brittle fracture morphology. In L5 (Fig. 6b and c, OM), the FPZ extends toward the adjacent hole, where interaction between the crack tip and the hole leads to overlapping stress fields and concentrated deformation, thereby promoting localized crack initiation. In L5 with W/D = 6.6 (Fig. 6b–OM), stable crack growth occurred near the crack tip with slight irregular damage toward the hole, indicating reduced stress field overlap. In contrast, W/D = 3.3 (Fig. 6c) showed the FPZ extending toward the hole, while the edge region exhibited limited stable growth and smearing fracture of slip surface. These results show that crack tip - hole interaction concentrated the stress field, forming a highly localized FPZ that accelerated failure. As L increases, the crack tip - hole interaction progressively decreases, altering the crack propagation pattern (Fig. 7). For W/D = 3.3 at L10 (Fig. 7b), OM images show the FPZ still forms at the crack tip, but its extension toward the hole—prominent in L5—is suppressed, producing a more balanced stable-growth distribution across the width. At L15 and L20, the FPZ–hole overlap becomes negligible, and crack behavior approaches the no-hole case with the maximum load nearly recovered. For W/D = 6.6, the FPZ forms in a stable, uniform manner regardless of L, resulting in predictable crack initiation and propagation. In contrast, for W/D = 3.3, FPZ formation is unstable, leading to irregular crack paths and greater variability in slip locations. In L15, L20, off-axis damage occurred around the hole before crack propagation, and, as noted in Section 3.2.1, this deformation affected material properties.

Regardless of the OH configuration, once the crack passes through the hole, its path deflects markedly toward the upper (compressive) side, producing a pronounced bump on the fracture surface (Figs. 6, 7 and 3D OM). this deflection results mainly from stress field redistribution and local concentration around the hole, which interrupt load transfer and distort the local shear field. In this study, the large property difference between tensile and compressive directions in unidirectional laminates further intensified stress concentration at the hole ends, making slip-induced fracture more likely to curve the compressive side. Similar behavior has been reported in previous tensile and compressive tests on open-hole composites [12,16].

3.2.3. *Influence of geometry and temperature on mode II behavior*

The Mode II behavior of OH specimens at 110 °C and 150 °C (Fig. 8) indicates that increasing temperature promotes the crack initiation load and shifts the fracture mode from slip to stable growth, with this change depending on both W/D and L. At 110 °C, the L5 specimen (Fig. 8a) exhibited extended stable crack propagation, unlike the no-hole specimens, which were slip-dominated at 25 °C and only briefly stable at 110 °C (Section 3.1). In L5 W/D = 6.6, the crack propagated stably along the ligament (■→▲ in Fig. 8a DIC), followed by a short slip. In W/D = 3.3, the load temporarily recovered during propagation (after ▲), due to increased path resistance by bump formation (ref. Fig. 9). As the propagating crack approached the loading point, additional bending failure occurred around the hole, resulting in a rapid load drop. In contrast, the L15 displayed an extended slip region, similar to the 110 °C no-hole specimen, suggesting lower sensitivity to the hole.

This slip behavior generally occurs when the crack rapidly reaches the FPZ with high strain energy, leading to interfacial failure [49]. For L5, the short ligament and irregular FPZ formation caused intermittent energy release, which contributed to maintaining stable crack growth. Overall, crack tip–hole interaction accelerates initiation. However, elevated temperatures also promote stable crack propagation, thereby mitigating the risk of catastrophic failure. W/D = 6.6 and 3.3 exhibited crack initiation loads 11.6 % and 27.1 % lower than the no-hole condition (Fig. 8c), showing a more pronounced reduction compared to 25 °C (−5.4 % and −19.1 %). This enhanced sensitivity to the OH configuration at elevated temperature is attributed to matrix softening, which diminishes load transfer efficiency and interfacial resistance,

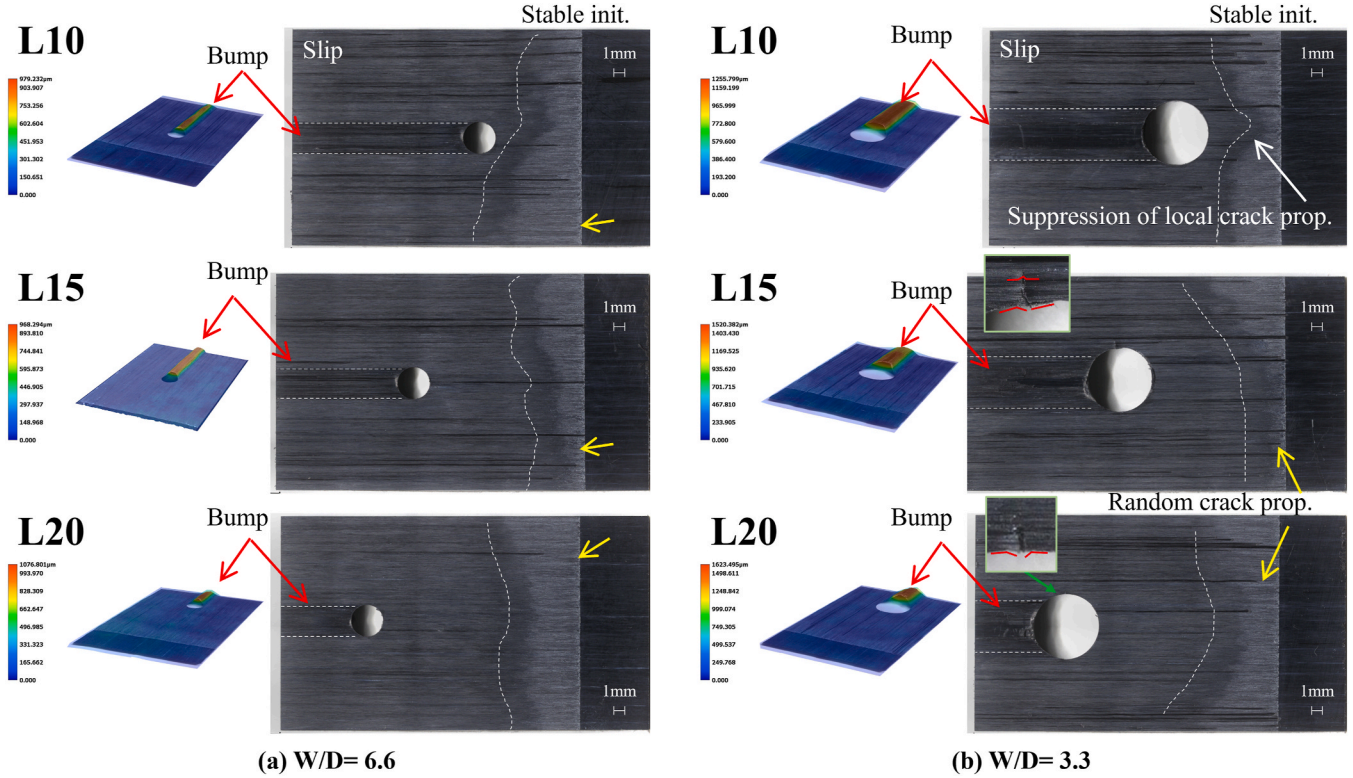

Fig. 7. Fracture surfaces of open-hole CF/PEKK specimens with increasing crack–hole distances at 25 °C, observed by optical microscopy: (a) W/D = 6.6, (b) W/D = 3.3.

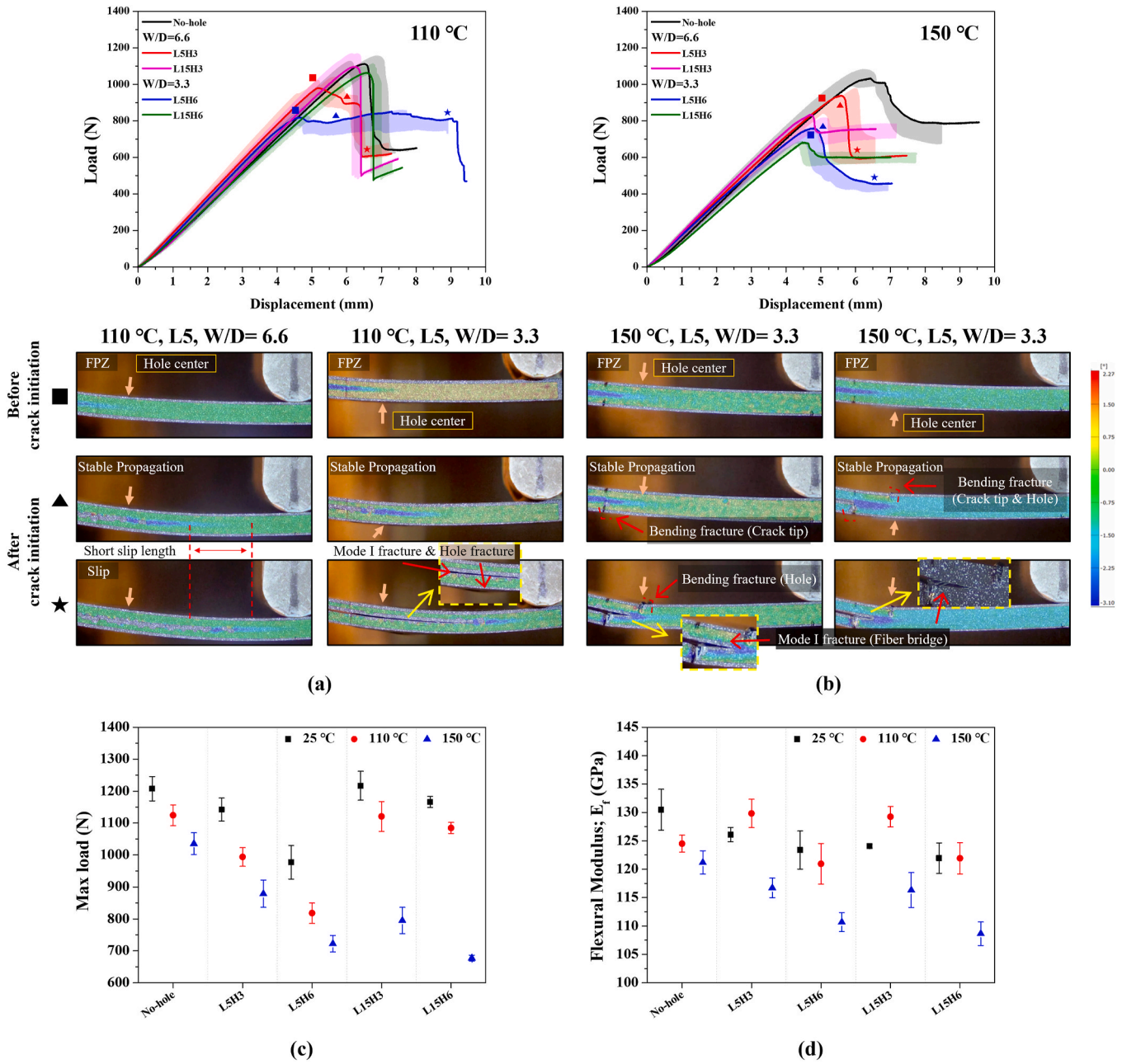

Fig. 8. Mode II behavior of CF/PEKK composites under different geometric configurations (W/D, L) and temperatures (110 °C, 150 °C): (a,b) load–displacement curves and DIC results at key points, (c) maximum load, and (d) flexural modulus.

thereby promoting earlier crack initiation even under comparable geometric stress conditions.

At 150 °C, L–D curves (Fig. 8b) exhibited a different pattern compared to 25 °C and 110 °C. The load decreased more gradually and maintained a high residual load capacity, indicating a stable fracture behavior. In the L5 specimen (DIC result), crack initiation was accompanied by localized bending near both the crack tip and the hole. This bending failure resulted from stress redistribution around OH, where elevated temperature lowered local stiffness and induced out-of-plane deformation under shear. As a result, delamination progressed in a mixed-mode manner (Mode I + II). L15 failed at lower load, dominated by bending fracture near the hole without crack initiation. As shown in Fig. 8d, the E_f generally decreased with increasing temperature and decreasing W/D ratio. However, an exception was observed at 110 °C for W/D = 6.6, where E_f increased. This indicates that E_f depends not only on thermal degradation but also on the extent and location of load transfer and distribution [16,50–52]. At 110 °C, partial matrix softening promoted stress redistribution near the tip and the hole, suppressing crack deflection and post-hole bump formation (Fig. 9b and c). Consequently, a more uniform stress field developed around the tip and the hole, local energy absorption/redistribution increased [53], and the reduction in E_f was mitigated. At 150 °C, full softening near T_g caused localized failure near the hole, preventing stress redistribution and blocking load transfer. This effect was more pronounced with smaller W/D or larger L, sharply reducing E_f.

3.2.4. *Temperature and geometry-dependent failure behavior*

This section builds on the temperature-dependent behavior discussed in Section 3.2.3, focusing on geometry-specific fracture features and damage mechanisms in OH configurations under elevated temperatures (Figs. 9 and 10). With increasing temperature, stable crack propagation after initiation became predominant across all conditions, consistent

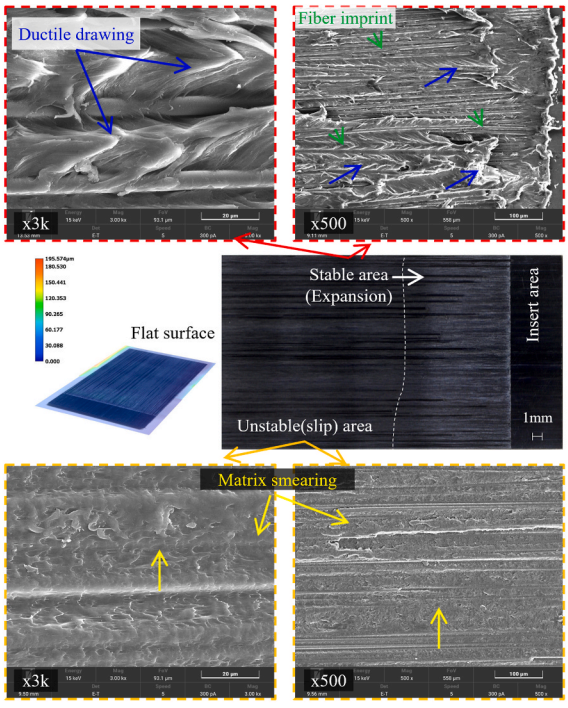

(a) 110°C No-hole

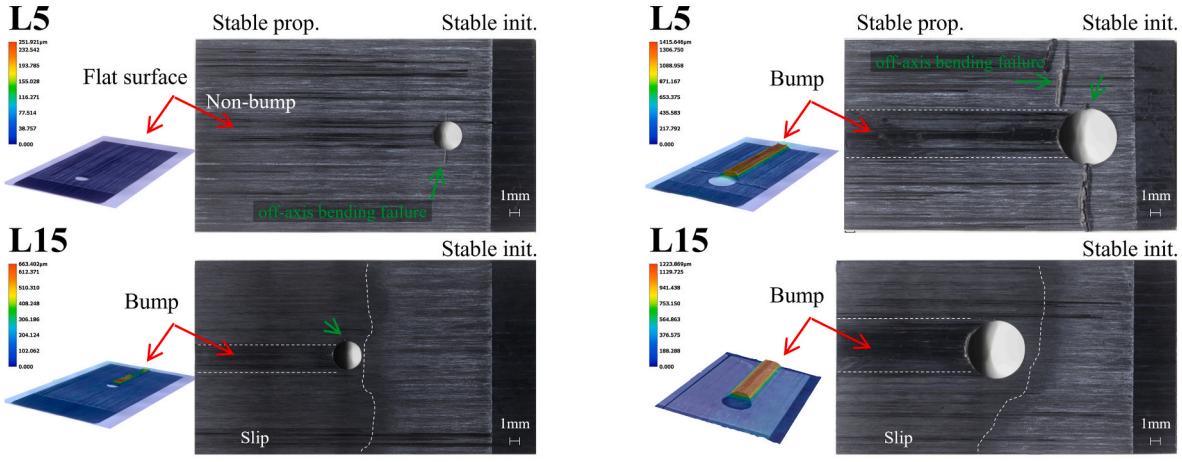

(b) 110°C, W/D= 6.6 (c) 110°C, W/D= 3.3

Fig. 9. Fracture surfaces of CF/PEKK specimens with different open-hole geometries at 110 °C, observed by OM and SEM: (a) no-hole, (b) W/D = 6.6, (c) W/D = 3.3 (b, c: OM results only); elevated temperature promotes stable propagation with ductile drawing in the FPZ; bump formation varies with crack-propagation mode.

with the L–D curve trends shown in Fig. 8a. In the initial FPZ region, the matrix showed more ductile drawing than at 25 °C, highlighting enhanced ductility and promoting stable crack growth (Fig. 9a). After passing through the hole, differences in slip behavior and bending failure were observed depending on W/D. For W/D = 3.3, bending failure around the hole gradually developed and led to abrupt failure, whereas for W/D = 6.6, only minor bending failure occurred, accompanied by a short slip. This is attributed to reduced ligament integrity at high temperature, facilitating failure initiation under local stress concentration.

In the crack path, the W/D = 3.3 exhibited diffraction toward the hole's upper edge—similar to 25 °C—forming a bump. In contrast, W/D = 6.6 showed neither diffraction nor bump formation when passing through the hole; however, in L15, slip occurred just before reaching the hole, causing the crack deflection and bump. Elevated temperature relaxed the stress field around the hole and broadened the shear deformation distribution, suppressing localized deformation. As W/D increased, the wider ligament redistributed stress from a localized zone to a larger area, reducing geometric stress concentration effects [12,14]. The stress field did not disappear, and fracture patterns still depended on crack propagation behavior: under stable propagation, the crack passed slowly, allowing the stress field to be further alleviated and redistributed over a wider region.; under slip-induced rapid propagation (e.g., L15), redistribution was limited, and the crack followed the pre-existing concentrated stress path at the hole's upper edge, forming a bump.

At 150 °C, fracture was predominantly mixed-mode (Mode I + II) with a bending-dominated response (Fig. 10), consistent with the temperature-dependent trends described in Section 3.2.3. In L5 (Fig. 10b and c), bending failure develops ahead of the crack tip and the hole, but no bending damage appeared along the hole line at the crack tip. This localized failure divides two regions: region A (off-axis from the hole line) and region B (between the crack tip and hole). Visual and SEM inspections reveal clear differences in matrix morphology between these zones: In region B, the matrix exhibited sharp vertical Mode I-like fracture features, resembling mixed-mode delamination [54], while in

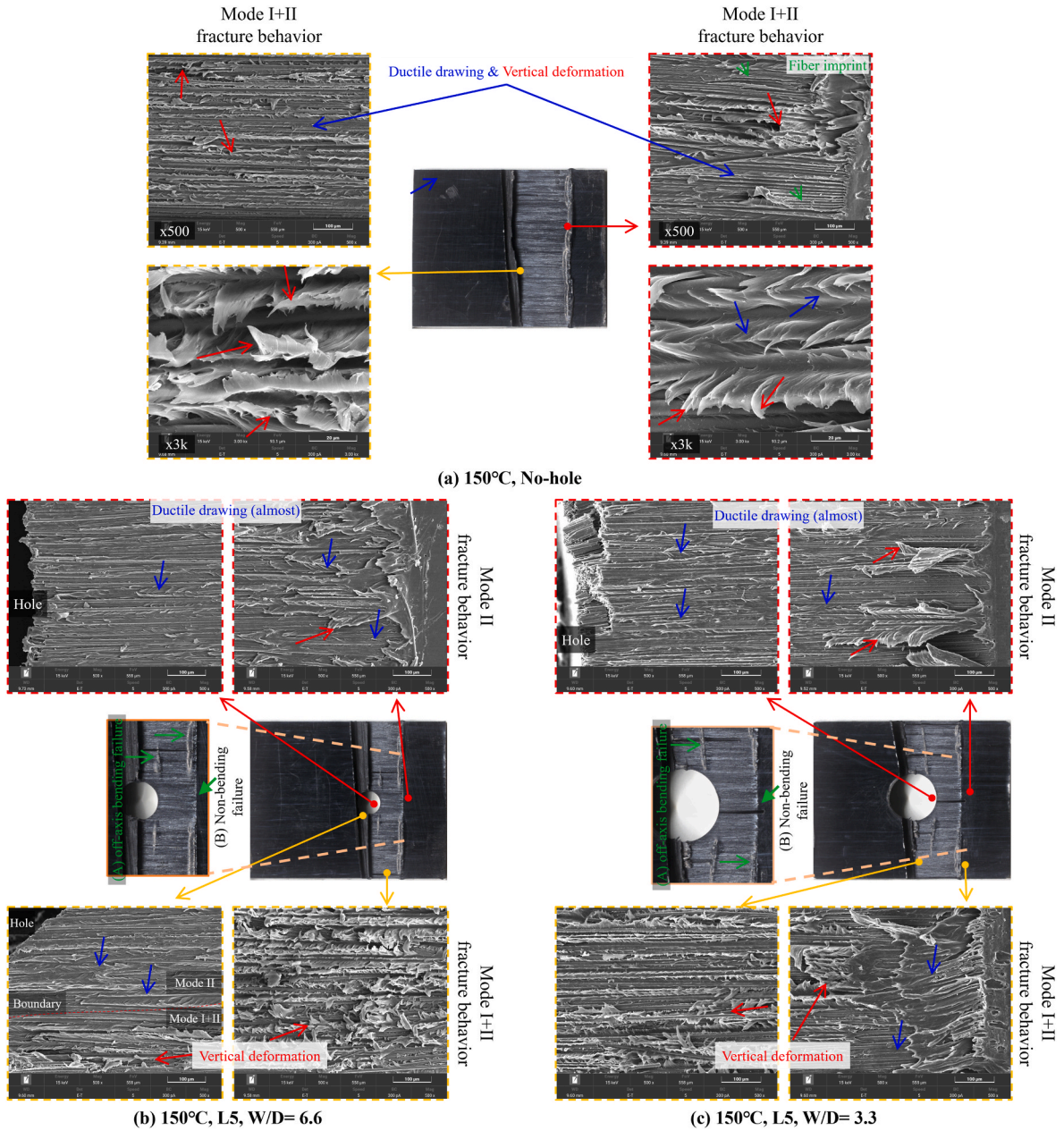

Fig. 10. Fracture surfaces of CF/PEKK specimens with different open-hole geometries at 150 °C, observed by OM and SEM: (a) no-hole, (b) L5, W/D = 6.6, (c) L5, W/D = 3.3; mixed-mode (I + II), bending-dominated response.

region A, a shear-dominated fracture similar to lower temperatures appeared.

For L15, where the hole is positioned farther from the crack tip, stress field interactions are negligible, and only localized bending failure is observed near the hole without delamination. These results show that at elevated temperature, CF/PEKK fracture behavior is governed by the combined influence of thermal softening, geometric configurations (W/D, L), and slip occurrence. This interplay produces a mixed-mode fracture response that cannot be attributed to a single local mechanism. Thus, for high-performance CF/PEKK at high temperature, durability predictions and designs must consider both thermal sensitivity and geometry-induced effects.

3.2.5. *Geometry and temperature-dependent fracture toughness*

Fig. 11 summarizes the G_{IIc}^{app} and E_{abs} results for all geometric and temperature conditions: (a) G_{IIc}^{app} variation with W/D and L at 25 °C, (b) temperature effects for each configuration, and (c) E_{abs}. G_{IIc}^{app} was calculated using the CBBM, which incorporates changes in specimen compliance during crack growth, thereby capturing the combined effects of geometry and temperature directly from experimental data. E_{abs} was quantified as the area under the L-D curve up to crack initiation, correlating fracture resistance with pre-initiation energy dissipation [27,55].

At 25 °C (Fig. 11a), the influence of the OH geometry is most pronounced in the L5 configuration. For W/D = 3.3, G_{IIc}^{app} drops to 2.25 kJ/m^2 (68 % of the no-hole, 25 °C No-hole G_{IIc}^{app} = 3.32 kJ/m^2), while increasing W/D to 6.6 recovers G_{IIc}^{app} (2.99 kJ/m^2) to approximately 90 % of the no-hole. The influence of L is also clear from the results, as the crack–hole distance increases from L5 to L20, G_{IIc}^{app} for W/D = 3.3 progressively recovers to 93 % (L10, 3.22 kJ/m^2), 106 % (L15, 3.58 kJ/m^2), and 104 % (L20, 3.4 kJ/m^2) of the no-hole. The increase at L15 aligns with reduced Mode II flexural modulus (Section 3.2.1) and higher

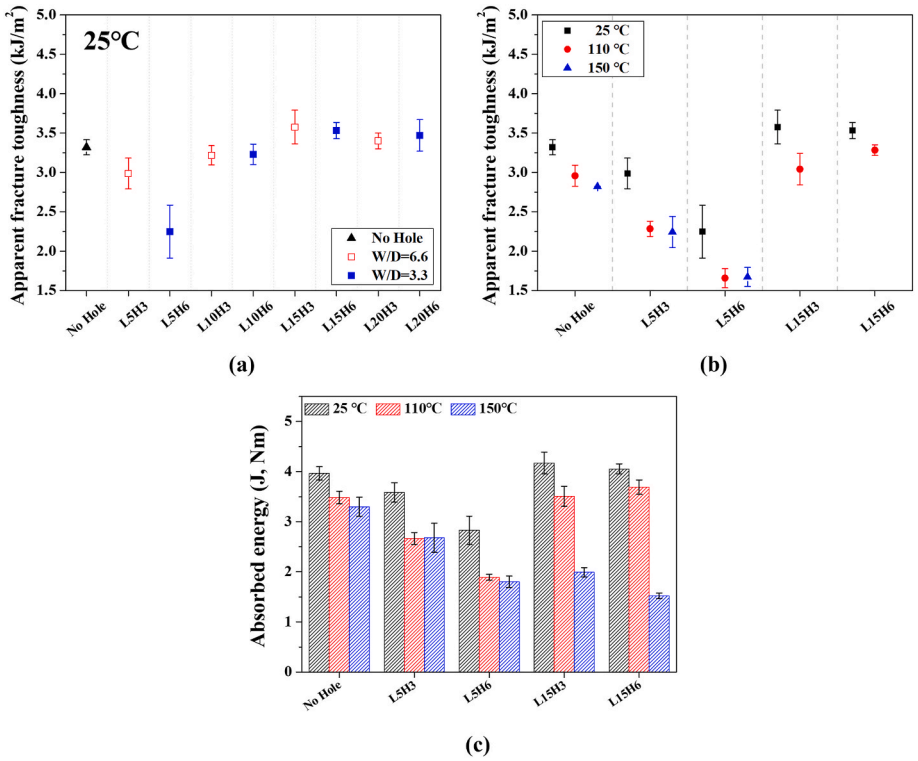

Fig. 11. Fracture characteristics of open-hole CF/PEKK specimens: (a) apparent fracture toughness (G_{IIc}^{app}) for various open hole geometries at 25 °C, (b) G_{IIc}^{app} under different temperature and geometric conditions, and (c) energy absorbed up to crack initiation for various temperatures and geometries.

accumulated energy (Fig. 11c), enhancing fracture resistance.

Temperature effects (Fig. 11b) showed that at 110 °C, L5 with W/D = 6.6 retained ~77 % of no-hole (110 °C No-hole G_{IIc}^{app} = 2.96 kJ/m^2), while W/D = 3.3 retained 56 % of no-hole. These retentions, being lower than at 25 °C, indicate greater sensitivity to OH as temperature rises. For L15, G_{IIc}^{app} recovery with temperature was more pronounced. At 110 °C, W/D = 6.6 and 3.3 reached 102 % and 111 % of the no-hole, respectively, which is similar to the results at 25 °C. At 150 °C, which is close to T_g, interfacial shear performance generally degrades [3] and viscoelastic losses increase, so the effective energy accumulated up to crack initiation (E_{abs}) is unlikely to exceed that at 110 °C. Even so, in some configurations E_f was comparable to 110 °C (Fig. 11c). For L5, W/D = 6.6 and 3.3 specimens retained 79 % and 59 % of no-hole (150 °C No-hole G_{IIc}^{app} = 2.28 kJ/m^2), respectively, showing a trend similar to 110 °C (Fig. 11b). These results suggest that, at 150 °C, a substantial fraction of the accumulated energy is expended in sustaining and initiating local bending rather than directly contributing to interfacial shear for crack initiation; a mechanism in which local bending precedes crack growth and subsequently transitions to mixed-mode (Mode I + II) propagation is consistent with this interpretation. By contrast, for L15 at 150 °C, bending failure occurred without crack initiation, precluding the calculation of G_{IIc}^{app}. This suggests that at high temperature, deformation at the stress concentration around the hole precedes crack initiation, leading to global bending-dominated failure. Collectively, increasing W/D and ensuring sufficient crack–hole distance is key to limiting G_{IIc}^{app} reduction from open holes and minimizing temperature sensitivity in CF/PEKK composites.

3.3. Mode II properties of bolt jointed CF/PEKK

3.3.1. Influence of geometry and temperature on mode II behavior

As discussed in Section 3.2, the OH configuration generally had an adverse effect on Mode II fracture behavior. This section examines how bolt insertion alters this influence, focusing on differences between BJ and OH specimens under identical geometric configurations. At 25 °C, BJ specimens exhibited L-D behavior similar to that of the OH specimens; however, most of the lost capacity was recovered (Fig. 12a–d, black line). For L5, the maximum load of BJ specimens reached values nearly identical to the no-hole condition for both W/D ratios, with W/D = 3.3 recovering up to 95 % of the no-hole value. This recovery is attributed to the compressive preload by BJ, enhancing interfacial friction and delaying shear crack growth [56–58].

For E_f, a slight recovery was observed for W/D = 3.3 at L5, as the bolt clamping zone directly contacted the crack tip; however, no improvement was found at L15 due to the dominant effect of the narrow ligament. For W/D = 6.6, the wider ligament reduced the influence of net-section loss. Consequently, E_f changes at L5 were limited by crack–hole interference, whereas at L15, the wider ligament led to an increasing trend. These results indicate that, at room temperature, the BJ configuration can effectively mitigate the mechanical disadvantages of the OH structure, particularly when the crack–hole distance is short and the ligament width is sufficient.

The effects of BJ configurations under 110 °C and 150 °C are illustrated in Fig. 12 by the red and blue lines, respectively. BJ specimens exhibited L–D curves similar to those of OH specimens but with varying reinforcement effectiveness. At 110 °C, L5 with W/D = 3.3 recovered ~80 % of the no-hole maximum load, whereas W/D = 6.6 retained 94 % and showed an extended post-yield plateau, indicating delayed crack propagation despite partial matrix softening (ref. Fig. 12d). At 150 °C, the maximum load of BJ specimens increased all conditions, but bending-induced delamination dominated, similar to OH specimens. For L15, local bending failure around the hole was predominant, and the BJ compressive stress delayed fiber damage onset, increasing the load-bearing capacity [59].

For E_f (Fig. 12f), geometric trends were similar at both temperatures. For W/D = 6.6, E_f remained high across L5 and L15, while W/D = 3.3 generally showed lower values, especially when the ligament was narrow or the hole was close to the loading point. At 110 °C, E_f of W/D = 3.3

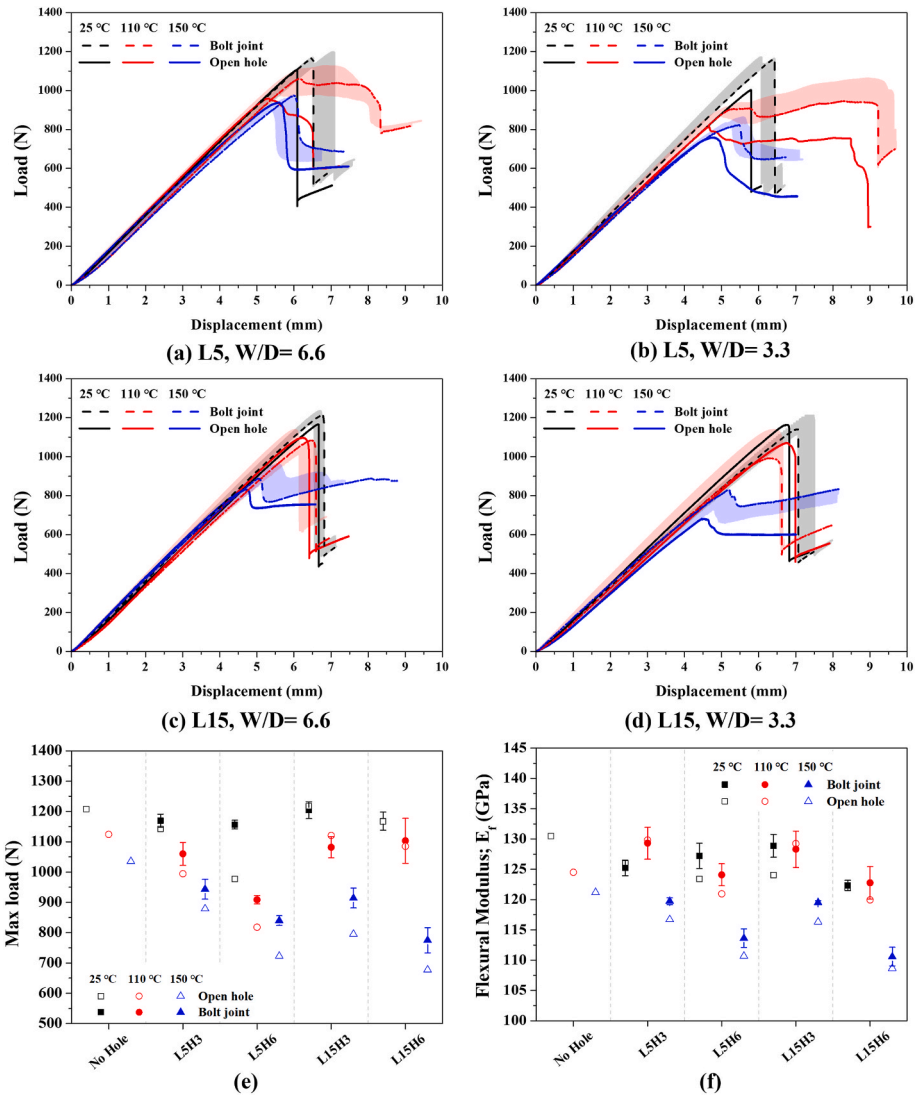

Fig. 12. Mode II test results of CF/PEKK specimens with open-hole and bolted-joint configurations at 25 °C, 110 °C, and 150 °C: (a–d) load–displacement curves for each condition, (e) maximum load, and (f) flexural modulus.

nearly matched the no-hole condition at L5 due to direct bolt–crack tip interaction. At 150 °C, E_f recovery diminished as matrix softening and bending failure dominated. These findings indicate that while BJ configurations consistently improve load-bearing capacity over OH specimens at elevated temperatures, the magnitude of improvement depends strongly on W/D, L, and the dominant fracture mode. Partial matrix softening at 110 °C allows the bolt to effectively stabilize crack growth, whereas at 150 °C, the prevalence of bending failure reduces the bolt's influence on Mode II resistance.

3.3.2. *Geometry and temperature on fracture behavior*

Under Mode-II loading, the mode II characteristic is governed by shear deformation and interfacial sliding. Energy-dissipation mechanisms—microcracking, fiber–matrix debonding, fiber bridging, and frictional sliding—delay crack growth and increase G_{IIc}^{app} [60,61]. Within the bolt-joint zone (BJZ), through-thickness compressive constraint suppresses local opening and slip around the hole and, together with frictional clamping, strengthens the interfacial-shear property, thereby partly offsetting OH-induced losses in Mode-II performance [62,63].

Fig. 13 presents the fracture surfaces of BJ specimens at 25 °C for different geometric configurations. Across all conditions, similar to OH specimens, a stable crack-propagation region developed near the crack tip due to FPZ formation, followed by slip. And, BJ specimens exhibited a distinct morphological zone around the hole—the BJZ—formed by local compressive stresses. Fractographic analysis further showed that, as the crack traversed the BJZ, ductile drawing—typical of OH specimens—was suppressed. instead, plastic deformation and matrix smearing dominated, and fiber exposure was frequently observed. These observations align with Catalanotti et al. [62]. Under Mode II loading, the compressive constraint within the BJZ that enhances load-bearing capacity and interfacial shear response may also promote fiber fracture, indicating a common underlying mechanism.

For L15, W/D = 6.6 specimens maintained a uniform BJZ shape, whereas W/D = 3.3 specimens exhibited a comparatively irregular circular pattern. This difference is attributed to non-uniform bending deformation induced by the OH configuration, suggesting that W/D plays a significant role in Mode II behavior. Within the BJZ, slip occurred before crack arrival, resulting in smearing as the predominant failure mode and thereby limiting the crack-arresting effect against slip. Additionally, in all conditions, the BJ configuration suppressed the formation of the bump observed in OH specimens. This suppression is attributed to the effective restriction of tensile damage around the hole by local compressive stress, which reduced crack deflection and promoted the formation of a flatter, shear-dominated, and more stable fracture surface [64].

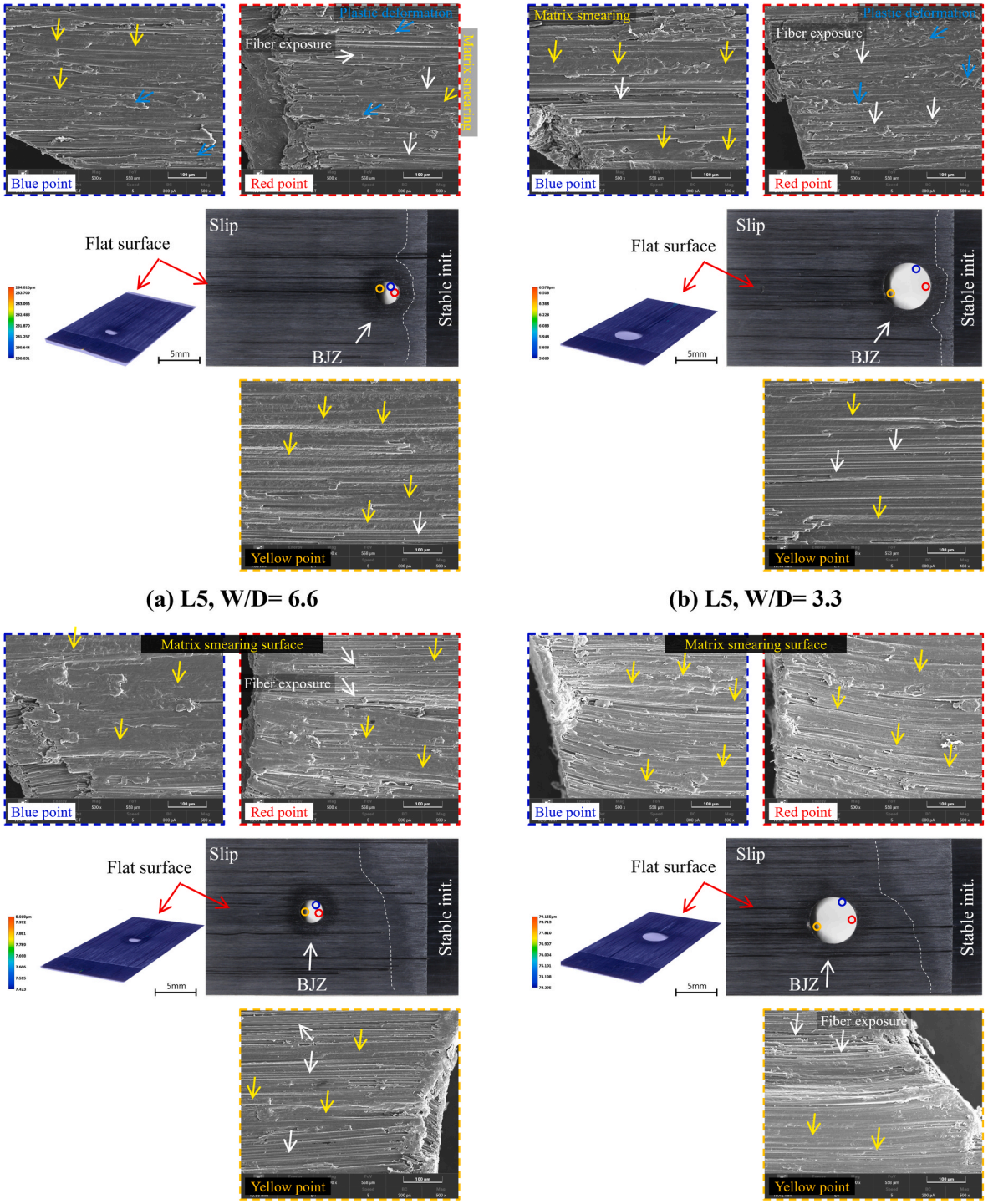

Fig. 13. Fracture surfaces of CF/PEKK specimens with different bolted-joint configurations at 25 °C, observed by OM and SEM at selected points (blue, red, yellow points); BJZ formation enhances interfacial properties, suppresses crack initiation and OH-type bump formation, with limited crack-arrest capability.

Fig. 14 and Fig. 15 present the differences in fracture surfaces of BJ specimens with different geometric configurations as the temperature increases. At 110 °C under the L5 condition, a greater amount of fiber fracture was observed within the BJZ compared with that at 25 °C, which is attributed to thermal degradation. This is associated with a limitation in the reinforcement effect on load-bearing capacity. In addition, for both W/D = 6.6 and 3.3, the off-axis bending failure around the hole observed in OH specimens was significantly delayed. This delay is attributed to the suppression of slip behavior for W/D = 6.6 and the mitigation of load drop for W/D = 3.3. For L15, the crack still propagated through the BJZ with slip, resulting in a limited crack-arresting effect. At 150 °C, similar to OH specimens, a mixed failure mode dominated by bending failure was dominant, and ductile drawing was frequently observed within the BJZ. Nevertheless, local bending fracture around the hole—commonly observed in OH specimens—was suppressed by the compressive forces in the BJZ, which, in some cases,

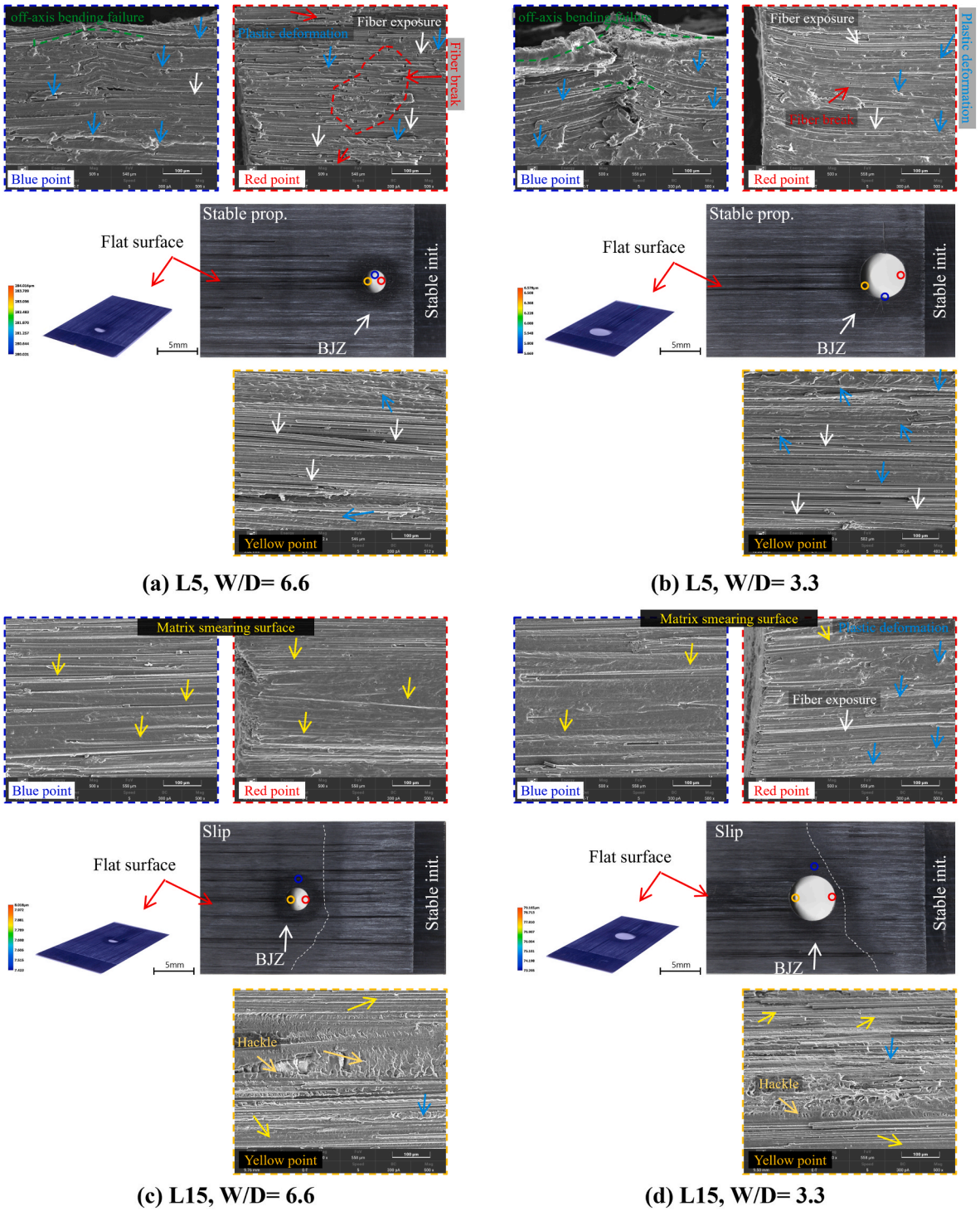

Fig. 14. Fracture surfaces of CF/PEKK specimens with different bolted-joint configurations at 110 °C, observed by OM and SEM at selected points (blue, red, yellow points); Thermal degradation increases fiber damage, while the stable propagation regime expands relative to 25 °C.

contributed to load retention and the formation of a stable crack path.

3.3.3. Effect of temperature and geometry-dependent fracture toughness

G_{IIc}^{app} and E_{abs} according to the BJ configuration are shown in Fig. 16. At 150 °C and L15, similar to the OH conditions, no crack initiation was observed, making it impossible to determine a valid G_{IIc}^{app}.

At 25 °C, the BJ specimen with L5 and W/D = 3.3 exhibited an approximately 39 % increase in G_{IIc}^{app} compared to the OH specimen (OH→BJ, 2.25–3.12 kJ/m^2), along with a 29 % recovery in E_{abs} (2.83–3.64 J). For W/D = 6.6, the increases were 15 % (2.99–3.43 kJ/m^2) and 12 % (3.59–4.01 J), respectively. In both cases, the performance was similar to that of the no-hole specimens, indicating the most significant reinforcement effect. In contrast, as L increased, the influence of BJ intervention on behavior other than stiffness became limited, resulting in E_{abs} values similar to those of OH and no-hole specimens, while G_{IIc}^{app} showed partial improvement.

With increasing temperature, for the L5, W/D = 6.6 condition, the recovery rates of G_{IIc}^{app} and E_{abs} relative to OH were 22 % (2.28–2.8 kJ/

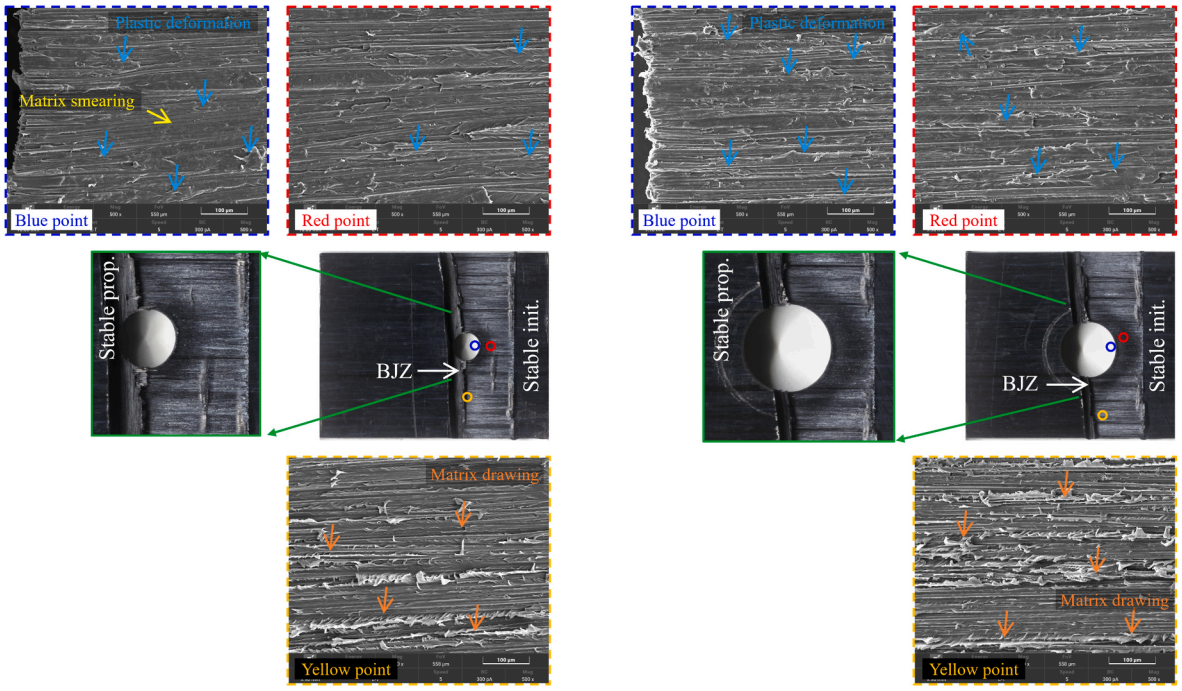

Fig. 15. Fracture surfaces of CF/PEKK specimens with different bolted-joint configurations at 150 °C, observed by OM and SEM at selected points (blue, red, yellow points); Transition to a mixed, bending-dominated failure mode.

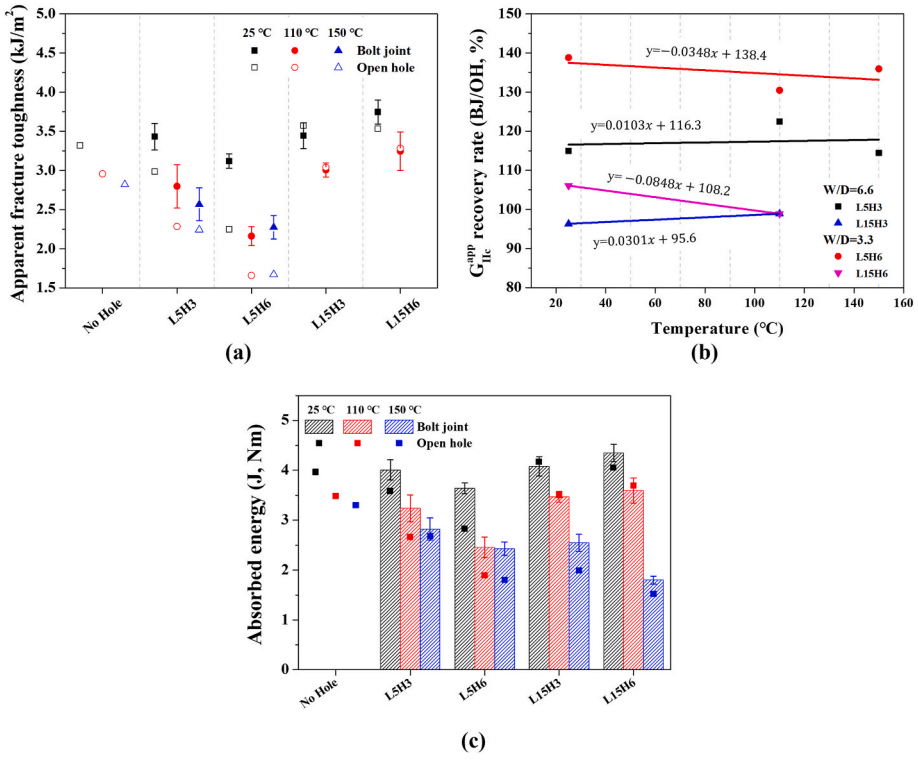

Fig. 16. Fracture characteristics of Bolted joint CF/PEKK specimens: (a) apparent fracture toughness and (b) absorbed energy up to crack initiation, both as functions of geometric configuration and temperature.

m^2) and 21 % (2.66–3.24 J) at 110 °C, and 14 % (2.24–2.57 kJ/m^2) and 5 % (2.67–2.82 J) at 150 °C, respectively. For W/D = 3.3, the recovery rates of both G_{IIc}^{app} and E_{abs} were 30 % (1.66–2.16 kJ/m^2, 1.89–2.46 J) at 110 °C and 35 % (1.67–2.27 kJ/m^2, 1.80–2.43 J) at 150 °C, showing a similar decreasing trend with temperature. As the temperature increased, the increments in E_{abs} and G_{IIc}^{app} became predominantly governed by the suppression of bending behavior. At 150 °C, bending became the dominant failure mode, and the reinforcement effect was

more pronounced when W/D was smaller or L was larger. In contrast, cases where the reinforcement effect decreased were attributed to crack initiation being relatively dominant in specimens with a wide ligament. Overall, the BJ structure generally improves fracture resistance; however, its effectiveness decreases under high temperature and small W/D conditions. This indicates that in CF/PEKK composites exposed to elevated temperatures, fracture behavior is highly sensitive to W/D, and that the interaction between W/D and failure mode near T_g is a key consideration in structural design.

4. Conclusion

This study investigated the effects of geometric configurations (W/D, L) and temperature (25 °C, 110 °C, 150 °C) on the Mode II and failure behavior of CF/PEKK composites with OH and BJ structures. The main findings are summarized as follows.

- The OH configuration directly affects the Mode II crack initiation, propagation path, and failure mode. Under W/D = 3.3, when the crack tip approaches the hole, the FPZ develops early and crack-tip–hole interaction (stress-field superposition) intensifies, promoting localized propagation; consequently, G_{IIc}^{app} decreases by up to 32 % relative to the no-hole specimen, indicating reduced damage resistance. Increasing L and W/D attenuates the interference with the crack tip, stabilizes crack initiation, and enables G_{IIc}^{app} and the maximum load to recover to 93–106 % of the no-hole reference. During propagation, stress-field imbalance around the OH induces deflection toward the compressive side, producing a bump-type morphology in the post-hole region.
- Rising temperature accentuates the viscoelastic response of CF/PEKK, thereby weakening Mode II crack-resistance. At 110 °C, the W/D = 3.3 configuration retains only ~56 % of the no-hole G_{IIc}^{app} at the same temperature, indicating lower retention than at 25 °C and highlighting temperature–hole interaction. Temperature also promotes stress redistribution around the hole. For W/D = 6.6, increased temperature suppresses post-hole crack deflection, leading to a partial recovery of E_f. At 150 °C (near T_g), matrix softening renders bending-assisted mixed-mode (Mode I + II) damage dominant, and crack-propagation behaviour becomes correspondingly more complex.
- The BJ configuration is effective in suppressing early failure and stabilising crack propagation under Mode II loading. Clamping introduces compressive confinement (preload and friction) at the interface, raising the crack-initiation threshold and suppressing post-hole deflection/slip-assisted propagation. Consequently, even for adverse geometry such as W/D = 3.3, the load-bearing capacity, G_{IIc}^{app}, and E_{abs} recover to ≥95 % of the no-hole reference, and the sensitivity to crack-tip–hole interaction is alleviated even at short L. With increasing temperature, the recovery diminishes somewhat; for example, at 110 °C G_{IIc}^{app} remains at ~80 % of the no-hole specimen, indicating that damage-mitigation persists at elevated temperature. Clamping also promotes load-path dispersion and stress redistribution, leading to more stable load transfer and suppressing the increase in compliance during propagation. Near 150 °C, mixed-mode and bending contributions become more pronounced, further limiting the recovery; nevertheless, the BJ configuration continues to inhibit crack growth/deflection and stabilize the fracture surface. Overall, BJ design provides a practical means to offset geometric vulnerabilities across W/D, L, and temperature, thereby enhancing mechanical performance, structural integrity, and high-temperature durability of CF/PEKK composite structures.
- This study quantified the Mode II behaviour of CF/PEKK laminates using an experiment-first approach, and we will verify and extend these findings through 3D simulation in subsequent work. Employing same-temperature, no-hole normalisation, we systematically reported G_{IIc}^{app}, failure behaviour, and mechanical characteristics (Load, E_f, compliance). These data can support future models by (i) calibrating temperature-dependent material parameters, (ii) specifying boundary conditions (clamping, ligament length, hole size), and (iii) defining validation targets (initial slope, maximum load, G_{IIc}^{app}–temperature trends, and crack paths). As a first step, results at 25 °C with systematic variation of W/D and L enable geometry-only verification. Next, the compressive constraint introduced by bolted clamping (preload and friction) can be quantified to test whether the observed partial recovery of E_f and G_{IIc}^{app} is reproduced. With geometry fixed, a material-only analysis will then calibrate temperature-dependent PEKK laws at 25/110/150 °C and cross-validate model predictions against the present experiments, thereby separating and quantifying geometric and material contributions and their interaction.
- Through this utilisation, mechanisms of stress-field superposition, FPZ enlargement, and mixed-mode transition—driven by holes, ligament length, and bolt confinement—can be visualised, yielding quantitative metrics and maps that translate into geometric-temperature–BJ clamping design guidelines for practice.

CRediT authorship contribution statement

Kyo-Moon Lee: Writing – review & editing, Writing – original draft, Visualization, Validation, Methodology, Investigation, Formal analysis, Data curation, Conceptualization. **Sanjay Kumar:** Writing – review & editing, Investigation, Conceptualization. **Sung-Won Yoon:** Writing – review & editing, Resources. **Chang-Wook Park:** Writing – review & editing, Investigation. **Nao-Aki Noda:** Writing – review & editing. **Yun-Hae Kim:** Writing – review & editing, Supervision, Resources, Project administration, Funding acquisition.

Funding

This paper was conducted with the support of the Korea Planning & Evaluation Institute of Industrial Technology with the financial resources of the government (Ministry of Trade, Industry and Energy) in 2025. (RS-2024-00431591, Development of Technology for integration of 2.6m-class cargo door composite structure for aircraft).

This research was supported by Korea Institute of Marine Science & Technology Promotion(KIMST) funded by the Ministry of Oceans and Fisheries(2520000449)

Declaration of competing interest

The authors declare that they have no known competing financial interests or personal relationships that could have appeared to influence the work reported in this paper.

Data availability

Data will be made available on request.

References

[1] Y.-H. Kim, S. Kumar, K.-M. Lee, S.-Y. Kim, S.-W. Yoon, S.-Y. Bae, et al., Advancing carbon fiber and its composites technology: korea's strategic growth and innovation, Compos. B Eng. 296 (2025) 112266, https://doi.org/10.1016/j.compositesb.2025.112266.

[2] C. Yildirim, H. Ulus, B. Beylergil, A. Al-Nadhari, S. Topal, M. Yildiz, Tailoring adherend surfaces for enhanced bonding in CF/PEKK composites: comparative analysis of atmospheric plasma activation and conventional treatments, Compos Part A Appl Sci Manuf 180 (2024) 108101, https://doi.org/10.1016/j.compositesa.2024.108101.

[3] C. Yildirim, H. Ulus, H.S. Sas, M. Yildiz, Evaluating the influence of service conditions on the out-of-plane and in-plane loading performance and damage behavior of unidirectional CF/PEKK composites for aerospace applications, Compos. B Eng. 304 (2025) 112637, https://doi.org/10.1016/j.compositesb.2025.112637.

[4] Y.-H. Kim, S. Kumar, X. Li, S.-Y. Kim, D.-H. Shin, Temperature-dependent mechanical properties and material modifications of carbon fiber composites for optimized structures in high-end industrial applications, Compos. B Eng. 303 (2025) 112602, https://doi.org/10.1016/j.compositesb.2025.112602.

[5] B. Kwon, W. Choi, H. Ju, J.-H. Kweon, Y.-W. Nam, Effects of consolidation processing parameters on the surface morphology and void content of braided thermoplastic composite tubes, Functional Composites and Structures 3 (2021) 035004, https://doi.org/10.1088/2631-6331/ac199f.

[6] Z. Cao, M. Cardew-Hall, Interference-fit riveting technique in fiber composite laminates, Aerosp Sci Technol 10 (2006) 327–330, https://doi.org/10.1016/j.ast.2005.11.003.

[7] F.S. Wang, X.S. Yu, S.Q. Jia, P. Li, Experimental and numerical study on residual strength of aircraft carbon/epoxy composite after lightning strike, Aerosp Sci Technol 75 (2018) 304–314, https://doi.org/10.1016/j.ast.2018.01.029.

[8] L. Li, L. Sun, T. Wang, N. Kang, W. Cao, Repeated low-velocity impact response and damage mechanism of glass fiber aluminium laminates, Aerosp Sci Technol 84 (2019) 995–1010, https://doi.org/10.1016/j.ast.2018.11.038.

[9] M.R. Abir, T.E. Tay, M. Ridha, H.P. Lee, On the relationship between failure mechanism and compression after impact (CAI) strength in composites, Compos. Struct. 182 (2017) 242–250, https://doi.org/10.1016/j.compstruct.2017.09.038.

[10] L.J. Hart-Smith, Design and analysis of bolted and riveted joints in fibrous composite structures. Recent Advances in Structural Joints and Repairs for Composite Materials, Springer Netherlands, Dordrecht, 2003, pp. 211–254, https://doi.org/10.1007/978-94-017-0329-1_7.

[11] S. Ekşi, L. Salman, M.F. Beşiroğlu, M. Memişoğlu, Open hole strength and damage behavior of GFRP and CFRP composites, Eng. Fail. Anal. 176 (2025) 109584, https://doi.org/10.1016/j.engfailanal.2025.109584.

[12] Z.C. Su, T.E. Tay, M. Ridha, B.Y. Chen, Progressive damage modeling of open-hole composite laminates under compression, Compos. Struct. 122 (2015) 507–517, https://doi.org/10.1016/j.compstruct.2014.12.022.

[13] R. Higuchi, T. Okabe, T. Nagashima, Numerical simulation of progressive damage and failure in composite laminates using XFEM/CZM coupled approach, Compos Part A Appl Sci Manuf 95 (2017) 197–207, https://doi.org/10.1016/j.compositesa.2016.12.026.

[14] F.P. van der Meer, L.J. Sluys, Mesh-independent modeling of both distributed and discrete matrix cracking in interaction with delamination in composites, Eng. Fract. Mech. 77 (2010) 719–735, https://doi.org/10.1016/j.engfracmech.2009.11.010.

[15] O. Falcó, R.L. Ávila, B. Tijs, C.S. Lopes, Modelling and simulation methodology for unidirectional composite laminates in a Virtual Test lab framework, Compos. Struct. 190 (2018) 137–159, https://doi.org/10.1016/j.compstruct.2018.02.016.

[16] X. Li, S. Kumar, D.-W. Hwang, D.-H. Shin, S.-Y. Bae, Y.-H. Kim, Geometry and temperature effects on tensile properties and failure behaviors of open-hole and bolted-joint CF/PEKK composites, Compos Part A Appl Sci Manuf 185 (2024) 108336, https://doi.org/10.1016/j.compositesa.2024.108336.

[17] X. Li, S. Kumar, D.-W. Hwang, D.-H. Shin, Y.-H. Kim, Pin-loaded tensile behavior and failure analysis of CF/PEKK composites under extreme temperature, Compos Part A Appl Sci Manuf 175 (2023) 107823, https://doi.org/10.1016/j.compositesa.2023.107823.

[18] C. Ho, E. Cheung, Delamination Arrestment in Bonded-Bolted Composite Structures by Fasteners, 2016.

[19] C.H.E. Cheung, K.Y. Lin, Numerical analysis of fastener Delamination/Disbond arrest mechanism in aircraft composite structures, J Aircr 49 (2012) 630–635, https://doi.org/10.2514/1.C031616.

[20] J.J. van de Kerk, R.F.V. de Melo, G. Bastiani, M.V. Donadon, M.A. Arbelo, A numerical and experimental study of fasteners as a delamination arrest mechanism in composite laminates under mode I loading, Thin-Walled Struct. 191 (2023) 111047, https://doi.org/10.1016/j.tws.2023.111047.

[21] S. Ahmadi, A. Zeinedini, Experimental, theoretical and numerical investigation of the drilling effects on mode I delamination of laminated composites, Aerosp Sci Technol 104 (2020) 105992, https://doi.org/10.1016/j.ast.2020.105992.

[22] E. Jahanian, A. Zeinedini, Influence of drilling on mode II delamination of E-glass/epoxy laminated composites, Theor. Appl. Fract. Mech. 96 (2018) 398–407, https://doi.org/10.1016/j.tafmec.2018.06.002.

[23] M.D. Banea, LFM da Silva, Campilho Rdsg, Effect of temperature on tensile strength and mode I fracture toughness of a high temperature epoxy adhesive, J. Adhes. Sci. Technol. 26 (2012) 939–953, https://doi.org/10.1163/156856111X593649.

[24] J.P. Márquez Costa, Review of fracture characterization by delamination and debonding of polymer composite materials and bonded interfaces subjected to high temperature, Mech. Adv. Mater. Struct. (2025) 1–30, https://doi.org/10.1080/15376494.2025.2466075.

[25] Z. Yun, S. Zhu, L. Chen, X. Pan, J. Deng, H. Fan, et al., Mode I delamination propagation of thermoplastic composite laminate at different temperatures: experimental and numerical simulation, Compos. Struct. 363 (2025) 119096, https://doi.org/10.1016/j.compstruct.2025.119096.

[26] R. de CM. Sales, S.R. Gusmão, R.F. Gouvêa, T. Chu, J.M.F. Marlet, G.M. Cândido, et al., The temperature effects on the fracture toughness of carbon fiber/RTM-6 laminates processed by VARTM, J. Compos. Mater. 51 (2017) 1729–1741, https://doi.org/10.1177/0021998316679499.

[27] K.-M. Lee, S. Kumar, S.-Y. Kim, D.-H. Shin, C.-M. Wu, S.-Y. Bae, et al., Geometric effects on the fracture toughness and delamination behaviors of carbon fiber/polyetherketoneketone composites with open holes and bolted joints, Thin-Walled Struct. 210 (2025) 113045, https://doi.org/10.1016/j.tws.2025.113045.

[28] Moura Mfsf de, M.A.L. Silva, A.B. de Morais, J.J.L. Morais, Equivalent crack based mode II fracture characterization of wood, Eng. Fract. Mech. 73 (2006) 978–993, https://doi.org/10.1016/j.engfracmech.2006.01.004.

[29] M.B. Rossini, M.Z. Sadeghi, T. Quadflieg, T.A. Schneiders, T. Gries, K.-U. Schröder, Delamination assessment of a composite laminate interleaved with electrospun TPU fibers under Mode-I and Mode-II loading, Int J Adhes Adhes 117 (2022) 103007, https://doi.org/10.1016/j.ijadhadh.2021.103007.

[30] M.M. Arouche, M. Pavlovic, Experimental and numerical analysis of the effect of temperature on the mode I and mode II delamination of glass fiber woven composites, Compos. B Eng. 293 (2025) 112131, https://doi.org/10.1016/j.compositesb.2025.112131.

[31] M.A. Alexandre, E. Dantras, C. Lacabanne, E. Perez, S. Franceschi, D. Coudeyre, Effect of PEKK oligomers sizing on the dynamic mechanical behavior of poly(ether ketone ketone)/carbon fiber composites, J. Appl. Polym. Sci. 137 (2020), https://doi.org/10.1002/app.48818.

[32] Y.S. Yildirimoglu, F. Ozturk, Advances in mechanical and physicochemical performances of recycled carbon fiber reinforced PEKK composites, Polym. Bull. 81 (2024) 14453–14478, https://doi.org/10.1007/s00289-024-05403-w.

[33] K.D. Cowley, P.W.R. Beaumont, The interlaminar and intralaminar fracture toughness of carbon-fibre/polymer composites: the effect of temperature, Compos. Sci. Technol. 57 (1997) 1433–1444, https://doi.org/10.1016/S0266-3538(97)00047-X.

[34] L. Berger, W.J. Cantwell, Temperature and loading rate effects in the mode II interlaminar fracture behavior of carbon fiber reinforced PEEK, Polym. Compos. 22 (2001) 271–281, https://doi.org/10.1002/pc.10537.

[35] C. Yildirim, H. Ulus, H.S. Sas, M. Yildiz, Evaluating the influence of service conditions on the out-of-plane and in-plane loading performance and damage behavior of unidirectional CF/PEKK composites for aerospace applications, Compos. B Eng. 304 (2025) 112637, https://doi.org/10.1016/j.compositesb.2025.112637.

[36] B.D. Davidson, M. Kumar, M.A. Soffa, Influence of mode ratio and hygrothermal condition on the delamination toughness of a thermoplastic particulate interlayered carbon/epoxy composite, Compos Part A Appl Sci Manuf 40 (2009) 67–79, https://doi.org/10.1016/j.compositesa.2008.10.006.

[37] J.L. Thomason, L. Yang, Temperature dependence of the interfacial shear strength in glass–fibre polypropylene composites, Compos. Sci. Technol. 71 (2011) 1600–1605, https://doi.org/10.1016/j.compscitech.2011.07.006.

[38] H.S. Kim, W.X. Wang, Y. Takao, G. Ben, Effects of temperature on mode II fracture toughness of multidirectional CFRP laminates, Int. J. Mod. Phys. B 17 (2003) 1717–1723, https://doi.org/10.1142/S0217979203019563.

[39] J. Jeong, D. Lee, H. Ju, J. Kweon, Y. Nam, Effect of hygrothermal condition on single-lab shear behavior of induction-welded CF/PEKK thermoplastic composites, Adv. Compos. Mater. 32 (2023) 657–673, https://doi.org/10.1080/09243046.2022.2128267.

[40] Y. Gong, L. Jiang, L. Li, J. Zhao, An experimental and numerical Study of the influence of temperature on mode II fracture of a T800/Epoxy unidirectional laminate, Materials 15 (2022) 8108, https://doi.org/10.3390/ma15228108.

[41] Y. Gong, L. Jiang, H. Zhang, Z. Wang, N. Hu, Temperature effects on the mode II delamination propagation behavior of aerospace-grade CFRP multidirectional laminates, Mech. Adv. Mater. Struct. 31 (2024) 2170–2183, https://doi.org/10.1080/15376494.2022.2152143.

[42] B. Lan, Y. Liu, S. Mo, M. He, L. Zhai, L. Fan, Interlaminar fracture behavior of carbon Fiber/Polyimide composites toughened by interleaving thermoplastic polyimide fiber veils, Materials 14 (2021) 2695, https://doi.org/10.3390/ma14102695.

[43] R.S. Kumar, Mode-II interlaminar fracture of composite materials in the presence of randomly distributed defects, Int. J. Fract. 231 (2021) 201–221, https://doi.org/10.1007/s10704-021-00581-4.

[44] R.S. Kumar, Effects of randomly distributed defects on Mode-I interlaminar fracture of composite materials, Eng. Fract. Mech. 248 (2021) 107699, https://doi.org/10.1016/j.engfracmech.2021.107699.

[45] K. Mateusz, A. Henryk, G. Grzegorz, Stress distribution in a plate with a holes along the diagonal distribution under plane biaxial load, Strojnícky Časopis - Journal of Mechanical Engineering 70 (2020) 91–100, https://doi.org/10.2478/scjme-2020-0023.

[46] S.A. Kumar, R. Rajesh, S. Pugazhendhi, A review of stress concentration studies on fibre composite panels with holes/cutouts, Proc. Inst. Mech. Eng., Part L 234 (2020) 1461–1472, https://doi.org/10.1177/1464420720944571.

[47] L. Belgacem, D. Ouinas, J.A. Viña Olay, A.A. Amado, Experimental investigation of notch effect and ply number on mechanical behavior of interply hybrid laminates (glass/carbon/epoxy), Compos. B Eng. 145 (2018) 189–196, https://doi.org/10.1016/j.compositesb.2018.03.026.

[48] H.A.B. Alves, F.M. Monticeli, C.M.M. Lobo, M.Y. Shiino, Stress concentration in open hole laminate composites under bending: potential application in dental implant prosthesis, Mater. Res. 25 (2022), https://doi.org/10.1590/1980-5373-mr-2021-0235.

[49] M. Musafir, Z. Ameer, A. Hamzah, An experimental investigation of fracture modes and delamination behavior of carbon fiber reinforced laminated composite materials, Diagnostyka 24 (2023) 1–10, https://doi.org/10.29354/diag/156749.

[50] N. Boddeti, Y. Tang, K. Maute, D.W. Rosen, M.L. Dunn, Optimal design and manufacture of variable stiffness laminated continuous fiber reinforced composites, Sci. Rep. 10 (2020) 16507, https://doi.org/10.1038/s41598-020-73333-4.

[51] O. Fernandes, J. Dutta, Y. Pai, G. Pai D, Hole size influence on the open hole tensile and flexural characteristics of aramid-basalt/epoxy composites, Cogent Eng. 11 (2024), https://doi.org/10.1080/23311916.2024.2334911.

[52] X. Wang, A. Zhou, Y.H. Chui, Experimental investigation of Mode II fracture properties of parallel strand bamboo composite by end notched flexure test, Bioresources 14 (2019) 1579–1590, https://doi.org/10.15376/biores.14.1.1579-1590.
[53] M.G. Lee, K. Chung, C.J. Lee, J.H. Park, J. Kim, T.J. Kang, et al., The viscoelastic bending stiffness of fiber-reinforced composite Ilizarov C-rings, Compos. Sci. Technol. 61 (2001) 2491–2500, https://doi.org/10.1016/S0266-3538(01)00172-5.
[54] D.K. Too, S. Kumar, D.-H. Shin, Y.-H. Kim, Synergistic toughening of CFRP laminates using melt-infused thermoplastic interleaves and toughened epoxy, Compos. Commun. 53 (2025) 102192, https://doi.org/10.1016/j.coco.2024.102192.
[55] A. Manikkavel, V. Kumar, D.-J. Lee, Simple fracture model for an electrode and interfacial crack in a dielectric elastomer under tensile loading, Theor. Appl. Fract. Mech. 108 (2020) 102626, https://doi.org/10.1016/j.tafmec.2020.102626.
[56] M.R. Choudhury, K. Debnath, Experimental analysis of tensile and compressive failure load in single-lap bolted joint of green composites, Compos. Struct. 225 (2019) 111180, https://doi.org/10.1016/j.compstruct.2019.111180.
[57] F. Gamdani, R. Boukhili, A. Vadean, Tensile strength of open-hole, pin-loaded and multi-bolted single-lap joints in woven composite plates, Mater. Des. 88 (2015) 702–712, https://doi.org/10.1016/j.matdes.2015.09.008.
[58] A. Ataş, G.F. Mohamed, C. Soutis, Effect of clamping force on the delamination onset and growth in bolted composite laminates, Compos. Struct. 94 (2012) 548–552, https://doi.org/10.1016/j.compstruct.2011.08.014.
[59] Z. Qin, Y. He, S. Wang, C. Meng, Study on the influence of preload on the three-point bending limit load of CFPR countersunk bolt connections, in: M.A. Mellal, Y. Rao (Eds.), Third International Conference on Mechanical Design and Simulation (MDS 2023), SPIE, 2023, p. 69, https://doi.org/10.1117/12.2681956.
[60] S. Oshima, A. Mamishin, M. Hojo, M. Nishikawa, N. Matsuda, M. Kanesaki, High-resolution in situ characterization of micromechanisms in CFRP laminates under mode II loading, Eng. Fract. Mech. 260 (2022) 108189, https://doi.org/10.1016/j.engfracmech.2021.108189.
[61] C. Yildirim, H. Ulus, H.S. Sas, S. Topal, M. Yildiz, Assessing the fracture and dynamic mechanical performance of CF/PEKK joints bonded with epoxy-based adhesive film for aerospace applications: impact of thermal and cycling hygrothermal conditions, Compos Part A Appl Sci Manuf 190 (2025) 108659, https://doi.org/10.1016/j.compositesa.2024.108659.
[62] G. Catalanotti, C. Furtado, T. Scalici, G. Pitarresi, F.P. van der Meer, P.P. Camanho, The effect of through-thickness compressive stress on mode II interlaminar fracture toughness, Compos. Struct. 182 (2017) 153–163, https://doi.org/10.1016/j.compstruct.2017.09.014.
[63] Q. Bing, C.T. Sun, Effect of compressive transverse normal stress on mode II fracture toughness in polymeric composites, Int. J. Fract. 145 (2007) 89–97, https://doi.org/10.1007/s10704-007-9103-4.
[64] P. Ying, Y. Ying, R. Zhou, Z. Zhu, L. He, K. Yu, et al., The effect of normal compressive stresses on the fracture behavior of mode II crack under compression and shear loads, Theor. Appl. Fract. Mech. 130 (2024) 104347, https://doi.org/10.1016/j.tafmec.2024.104347.